2007

CAFM Studies of Epitaxial Lateral Overgrowth GaN Films

Vishal P. Kasliwal
Virginia Commonwealth University

CAFM Studies of Epitaxial Lateral Overgrowth GaN Films

A thesis submitted in partial fulfillment of the requirements for the degree of Master of Science in Physics/Applied Physics at Virginia Commonwealth University.

By

Vishal P. Kasliwal

B.S. in Physics and Mathematics

University of Richmond, 2005

M.S. in Physics/Applied Physics

Virginia Commonwealth University, 2007

Director: Alison. A. Baski, Associate Professor, Department of Physics

Virginia Commonwealth University,

Richmond, Virginia, 23284

April 29, 2007

Acknowledgments

I would like to thank a number of people for making this thesis possible. My advisor, Dr. A. Baski, mentored me, provided me with direction, purpose and did it all with the utmost patience. Without her, none of this would have been possible. I would also like to thank Dr. Morkoç of the EE department. His research group provided the samples used in this study. In addition, his class on semiconductor devices introduced me to the field. The two people directly responsible for the samples studied here are X. Ni and J. Xie. I have to thank them for the long hours that they spent in the EE cleanroom preparing these samples. Dr. Ü. Özgur and Dr. V. Avrutin provided critical thought and input on the work. Dr. J. C. Moore taught me how to use the AFM and was critical in helping me understand what I was doing. I would also like to thank my lab-mates, J. Ortiz, C. Baird, M. Johnson and M. Ruchala for their help in taking data and for making lab fun. Special thanks go to Matt and Jen for checking this document for errors. Most of all, I have to thank M. Willis for her invaluable help in getting to know the AFM.

Without the support of my family, this thesis would not have been possible. I dedicate this work to them. I'd also like to thank Katherine Bittner for her support and encouragement. Lastly, I'd like to thank my friends in Physics and outside for the fun I've had completing these last two years.

Table of Contents

List of Figures

Abstract

CAFM Studies of Epitaxial Lateral Overgrowth GaN Films

By Vishal P. Kasliwal, B.S.

A thesis submitted in partial fulfillment of the requirements for the degree of Master of Science at Virginia Commonwealth University. Virginia Commonwealth University, 2007.

Major Director: Alison A. Baski, Associate Professor, Department of Physics

This thesis uses the techniques of atomic force microscopy (AFM) and conductive AFM (CAFM) to study defect sites on GaN films. In particular, these defect sites demonstrate current leakage under reverse-bias conditions that are detrimental to device fabrication. Two growth techniques that were used to improve this leakage behavior for samples in this study included: epitaxial lateral overgrowth (ELO) and nano-ELO using a Si_3N_4 film. Both techniques decrease defects such as threading dislocations by controlling the nucleation and growth behavior of the GaN films. The ELO technique uses a patterned dielectric film to laterally grow micron-wide regions (referred to as 'wings') that minimize dislocation defects. Our CAFM studies indicate that ELO films have no detectable leakage sites in these wing regions; however, between these regions the films have typical leakage site densities seen for standard films on the order of 10^7 cm^{-3}. The nano-ELO technique utilizes a porous Si_3N_4 film to reduce defects over the entire film, and CAFM data indicate nearly a factor of ten reduction in leakage site densities. The nano-ELO technique is therefore optimal for an overall improvement in film quality, whereas the ELO technique is suitable for device fabrication in patterned regions with optimized film quality.

Chapter 1: Gallium Nitride and Conductive-AFM

1.1 Introduction

Gallium nitride is a widely studied semiconductor because of its desirable electrical and optical properties. GaN has a large direct bandgap of 3.4 eV at room temperature, leading to applications in high brightness LEDs, lasers, displays, detectors and high voltage amplifiers.[1] The synthesis of GaN was first performed in the early thirties by *Johnson* et al.[2], followed by the first epitaxial growth of GaN in the early sixties by *Maruska* and *Tietjen* using hydride vapor phase epitaxy (HVPE)[3]. Since then there has been considerable progress in the techniques of epitaxial growth of GaN using HVPE, metalorganic chemical vapor deposition (MOCVD), and molecular beam epitaxy (MBE). Unfortunately, native GaN substrates are not readily available, partly because of the low solubility of nitrogen in gallium, and also because of the high vapor pressure of nitrogen required at the growth temperature of GaN crystals. GaN must therefore be grown via heteroepitaxial methods on suitable substrates such as sapphire (Al_2O_3) and silicon carbide (SiC).

The growth of GaN thin films on non-native substrates results in a high density of threading dislocation crystallographic defects in the film's crystal structure due to a mismatch in the lattice constants.[1] Three types of threading dislocations may occur: edge, screw and mixed. These types are identified by what is termed the Burgers vector. A crystal may be visualized as consisting of planes of the constituent atoms. Though a Burgers vector is defined at a dislocation, it is best understood in the context of a dislocation-free crystal. Fig 1.1(a) shows a plane in a crystal with an edge dislocation. A closed path is traced around the defect using lattice vectors. The initial vector in the loop is marked in blue. The same lattice vectors are then used to trace a loop in an imaginary crystal plane without the edge dislocation. In this case, however, as shown in Fig 1.1(b), the path is no longer closed. The Burgers vector for the dislocation is then defined to be the closure failure of the path in (b) and is marked in green, and the dislocation line is the line of atoms along which the dislocation occurs. In Fig 1.1, the dislocation line for the edge defect shown in (a) would be perpendicular to the crystal plane. An edge dislocation occurs when the

crystal has a missing half-plane of atoms, resulting in the Burgers vector lying perpendicular to the dislocation line. A screw dislocation occurs when the atomic planes making up the crystal slip parallel to the direction of the plane to join the next plane, resulting in the Burgers vector lying parallel to the dislocation line. A screw dislocation may therefore be visualized as a helix. For a mixed dislocation, the Burgers vector is at an acute angle to the dislocation line. Studies that combine conductive atomic force microscopy (CAFM) and transmission electron microscopy (TEM) have shown that screw dislocations can exhibit leakage behavior under reverse-bias conditions.[4,5,6,7,8] Therefore, screw dislocations can adversely affect the behavior of devices and it is desirable to develop film fabrication techniques that reduce dislocation densities.

1.2 Crystal Structure of Gallium Nitride

Gallium nitride occurs in the form of three different crystal structures – wurtzite, zincblende, and rocksalt. The stable form under ambient conditions is the wurtzite form (hexagonal crystal structure), which the crystal structure for the samples studied in this work.[1] In the case of crystals that have a hexagonal structure, Bravais-Miller indices are used to denote the various directions in the crystal instead of Miller indices. The Bravais-Miller system uses four indices of the form [h k i l] where i = –h – k. The first three indices are related to the three-fold symmetry directions in the plane with hexagonal symmetry (see a_1, a_2, a_3 in Fig. 1.2), and the fourth index refers to the perpendicular "c" direction. An overview of some of the planes present in the hexagonal system is given in Fig 1.2. Letter-based names are oftentimes used to designate the most common planes and directions. The samples studied in this work are *a*- and *c*-plane GaN samples. The *c*-plane, or basal plane, is the most common plane for the growth of GaN films and is grown on *c*-plane sapphire. However, this plane suffers from internal spontaneous and strain-induced piezoelectric effects that produce strong electric fields.[9,10] The *a*-plane does not suffer from these constraints since it is non-polar, but it has a high density of twins.[1] In the case of MOCVD films, *a*-plane GaN is grown on *r*-plane sapphire.[11,12,13,14,15]

1.3 Experimental Techniques

The techniques of atomic force microscopy (AFM) and conductive AFM (CAFM) were used to study GaN samples prepared by the research group of Dr. Morkoç in the Department of Electrical Engineering at VCU. The AFM technique was invented in 1986 by Binnig and Gerber at IBM and Quate at Stanford University. An AFM uses a micro-machined cantilever with an integrated tip at the end that is scanned across a sample surface. The tip interacts with the sample via a variety of forces such as mechanical contact, Van der Waals, capillary, chemical bonding, etc. The subsequent deflections of the cantilever during the scanning process are modeled using Hooke's Law. These deflections are converted into force measurements by measuring the motion of a laser beam reflected off the backside of the cantilever onto a photodetector. To prevent sample damage during scanning, the tip is scanned across the surface with a constant tip-sample force using a feedback loop. A piezoelectric tube assembly is used to move the tube in the x, y and z directions.

Two primary modes exist for image acquisition: contact-mode and TappingMode™ AFM. In contact-mode imaging, the tip is held in contact with the sample at all times and a feedback loop maintains a constant tip-sample force. In tapping-mode imaging, the tip is oscillated at its resonant frequency while in close proximity to the sample. Tip-sample interactions lead to changes in the amplitude, frequency and phase of the tip's oscillation. A feedback loop then maintains a constant oscillation amplitude in order to obtain topographic information about the surface. In general, contact-mode AFM provides lower resolution than tapping-mode AFM, and may also cause degradation of the sample and tip. It is necessary to use contact-mode AFM imaging, however, when performing techniques such as conductive AFM that require tip-sample contact.

A schematic for an AFM with CAFM capabilities is shown in Fig 1.3. The sample is mounted on a sample disc and held by a magnetic sample holder on the chuck assembly. A laser is then aligned onto the cantilever by adjusting knobs on the top of the AFM head that move mirrors mounted inside the head. Lastly, the reflected laser beam is aligned onto the photodetector by adjusting knobs located on the left side of the AFM head. In tapping-mode

AFM, the resonant frequency of the tip is evaluated using preprogrammed routines. After that, the tip is lowered to the sample and imaging initiated. Image quality may be optimized by adjusting several parameters such as the amplitude setpoint, scan speed, scan angle, integral gain and proportional gain.

For this study, Ultrasharp μMasch NSC15 AIBS tips were used for all topographic imaging. These tips have a cantilever length of 125±5 μm, width of 35±3 μm and thickness of 4.0±0.5 μm. The resonant frequency of these tips lies in the range of 265 to 400 kHz with a typical value of 325 kHz, while the force constant is 20 to 75 Nm^{-1} with 40 Nm^{-1} being typical. The radius of curvature of the tip itself is less than 35 nm, while its height is between 15 to 20 μm. The full tip cone angle is less than 20°.

CAFM is a variant of contact-mode AFM in which a potential is applied to the sample, causing current to flow between the sample and a metallized tip. This current is measured and recorded along with the x-y position of the tip to create a "current" image of the surface. A topographic image is simultaneously acquired, allowing for a correlation between topographic and current-related features. Metal-coated Ti/Pt tips (μMasch NSC15) were used for CAFM measurements and Ohmic contacts were fabricated on the GaN films using a standard Ti/Al/Ti/Au metallization. The tip-sample current was measured using one of the following two commercial modules: tunneling atomic force microscopy module (TUNA™) or CAFM module. The TUNA module measures currents up to 100 pA with a sensitivity of ~1 pA, whereas the CAFM module measures larger currents up to 1 μA with a sensitivity of ~5 pA. The choice of the module used for a particular sample depends on the conductivity of the sample being examined. Note that the bias is applied to the sample while the tip is held at ground. Therefore, when a negative bias (or positive bias) is applied to an *n*-type GaN sample, then the tip-sample junction is under forward-bias (or reverse-bias) conditions. The VEECO Dimension 3100 AFM used in this study has an internal maximum voltage of 12 V; however, due to the poor conductivity of the samples in this study, the AFM was modified to apply an external voltage up to 120 V. This external bias was generated using a switchable battery pack in order to minimize noise levels.

Chapter 1 Figures

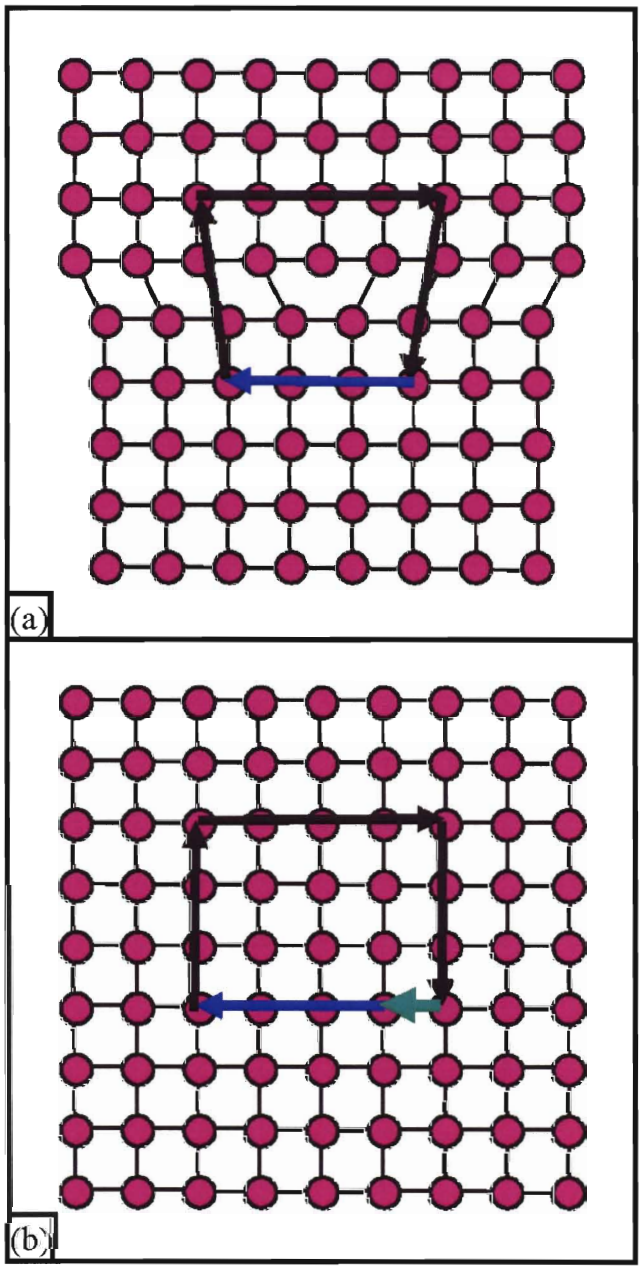

Fig 1.1: (a) An edge dislocation. (b) Ideal crystal structure used to define the Burgers vector (shown in green).

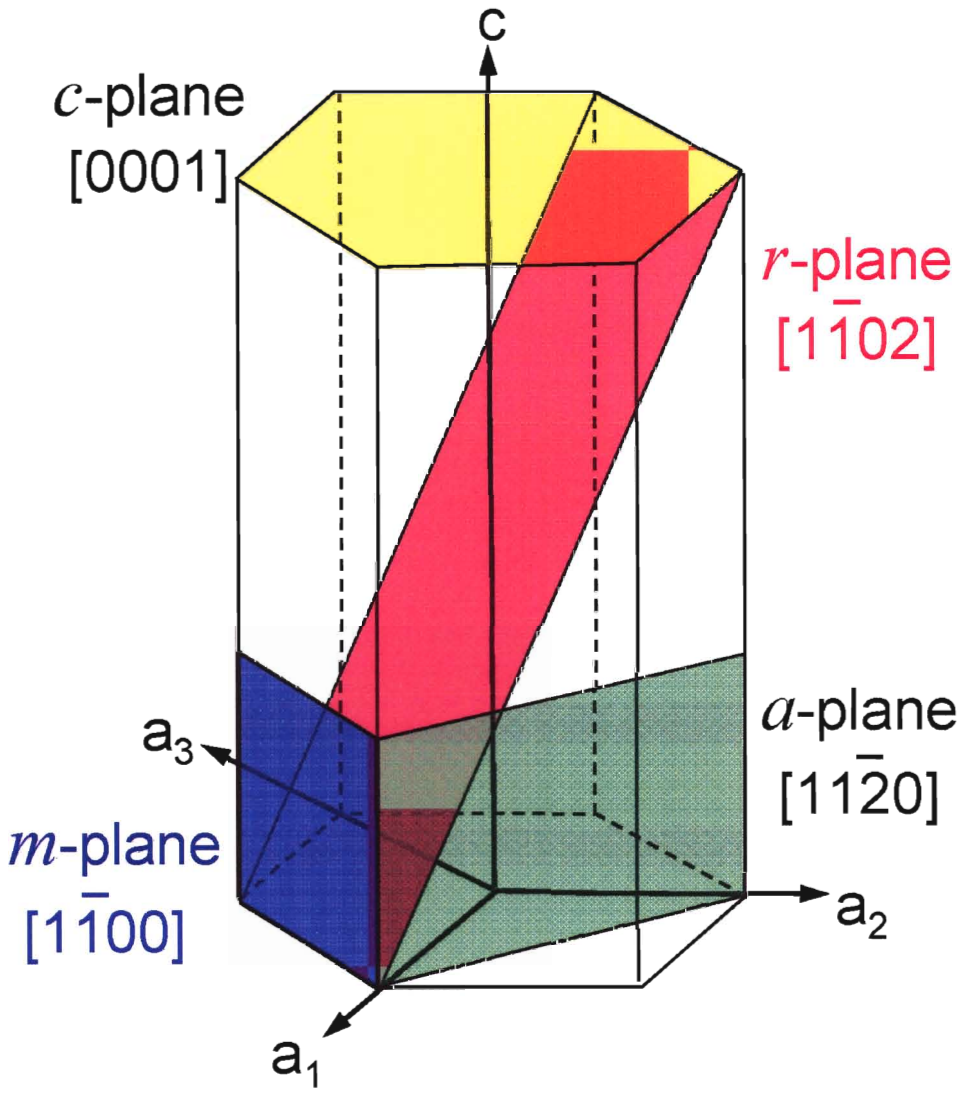

Fig 1.2: The major directions and planes in the hexagonal GaN system.

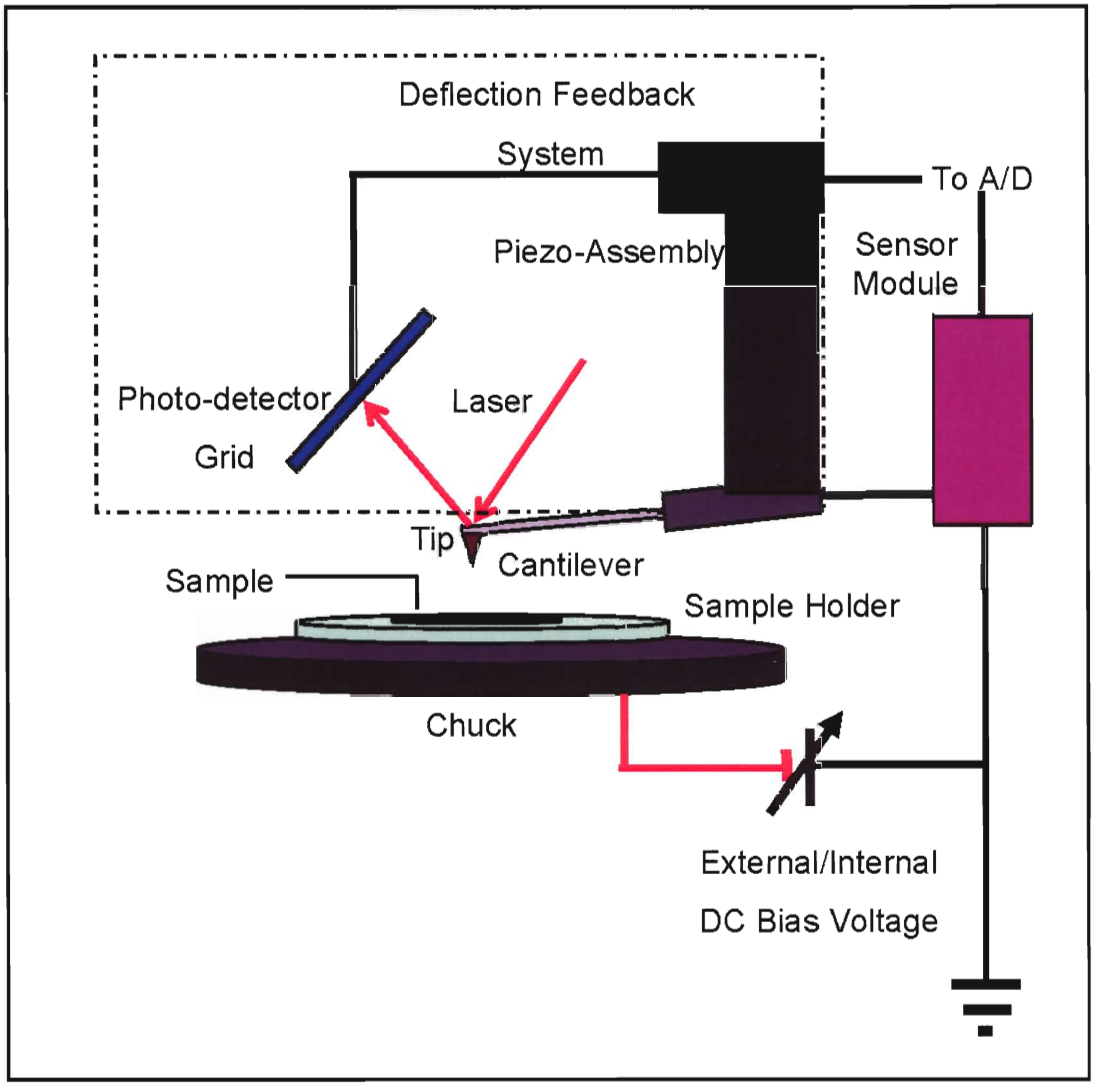

Fig 1.3: Schematic of AFM with C-AFM capability.

Chapter 2: Epitaxial Lateral Overgrowth

2.1 Introduction

As mentioned in Chapter 1, the heteroepitaxial growth of GaN on non-native substrates results in a large number of threading dislocations. The problem of reducing defect densities in GaN may be addressed by use of the epitaxial lateral overgrowth (ELO) technique. This technique is based upon the use of a dielectric mask with etched openings to reduce dislocation density above the mask by isolating the final GaN layer from the substrate layer.[16] As shown in Fig 2.1, the ELO technique starts by growing an initial GaN template layer on a substrate such as sapphire or SiC. A dielectric mask, usually SiO_2, is then deposited on the GaN template and etched to form a pattern of parallel stripes. Overgrowth is then performed until a coalesced GaN film is obtained. This is possible because *a*-plane GaN grows anisotropically, exhibiting a higher growth rate in the lateral *c*-direction. ELO growth achieves a low defect density because the GaN film nucleates in the windows and not on the dielectric mask. When the growth front reaches the top of the dielectric mask, lateral "wing" growth then occurs in the *c*-direction over the masked region until the film coalesces. In this manner, defects in the GaN template itself occur only in the window regions, while the wing region over the mask remains relatively defect free. The effect of the mask is to cause dislocations to bend out from the window region, resulting in a smaller number of surface-terminated threading dislocation densities in the window regions as compared to standard GaN films.[17,18,19] These dislocations may then either bend back towards the surface at the meeting front, or annihilate with dislocations from an adjacent window, almost eliminating surface-terminated threading dislocations in the wing regions. Studies have shown that GaN films grown via ELO using MOCVD or HVPE have reduced threading dislocation densities,[20,21,22,23] resulting in higher film quality with reduced dependence on substrate quality.[24,25]

In this study, four ELO samples were examined using CAFM to investigate their reverse-bias leakage defect behavior. The films were grown using a thin GaN nucleation layer (550 °C) followed by a thicker *a*-plane GaN layer (1.5 μm at 1050 °C).[26] For the ELO mask, a SiO_2 layer (100 nm) was then deposited on the template layer using plasma enhanced chemical vapor

deposition. A striped mask pattern aligned in the *m*-direction, was then transferred to the SiO_2 layer through conventional photolithography followed by a buffered oxide etch. The mask consisted of 20 or 10 μm–wide stripes of SiO_2 with 4 μm–wide spacings between them, resulting in a mask pitch of 24 or 14 μm. After completion of the ELO mask, the samples were then reloaded into the chamber for the overgrowth layer, where details of the growth conditions are presented in Table 2.1.

Of the four samples studied, two were found to be of higher quality as demonstrated by CAFM, X-ray diffraction (XRD), photoluminescence (PL), and near-field scanning optical microscopy (NSOM). In this work, these "higher quality" samples are referred to as H1 and H2, and the other two "lower quality" samples are referred to as L1 and L2. Sample H1 had a single-stage overgrowth which resulted in a height difference at the meeting front. Subsequently, it was found that a two-stage growth process reduced this difference by introducing a higher temperature during a second growth stage (1050 vs. 1000 °C). Samples H2 and L2 were grown with a lower III/V ratio than the other two samples to increase the photoluminescence quality; however, this decreases the lateral growth rate[27]. Sample L2 was grown under the same conditions as sample H2, but with *n*-type Si doping to enhance conductivity.

2.2 Topography of ELO GaN Films

The ELO samples demonstrated similar topography features such as striations along the *c*-direction and undulations along the *m*-direction, with window regions typically appearing as depressions (see Figs. 2.2 to 2.5). In general, there were also distinct differences in local topography for the wing vs. window regions. Using a Sobel edge-enhancement filter, it is possible to see that the window regions on most samples have a higher density of surface pits (~6 to 8 nm deep), which results in a higher surface roughness. Measurements on samples L1 and L2 indicate that the surface roughness is 1.4 times higher for the (lower quality) window regions than for the (higher quality) wing regions (see Table 2.1). Interestingly, it is not possible to distinguish the window and wing regions on sample H1 using AFM, most likely due to the thickness of the overgrowth layer. This sample also has the highest overall surface roughness (~20 nm). Lastly, sample H2 has the lowest overall surface roughness (<1.5 nm), as well as the

lowest window to wing ratio of surface roughness (1.1). The ratio of the window to wing surface roughness may therefore be correlated with sample quality.

In the wing regions, the Ga- and N-polar growth fronts meet and sometimes form a ridge at that meeting front [see Fig 2.6(c)]. This ridge is attributed to a miscut of the *r*-plane sapphire substrate, as well as to different tilt angles of the two growth fronts. The exact location of the meeting front is usually more prominent in CAFM images, because a higher density of leakage sites occurs at this location. Because it is known that the Ga-polar wing has a higher growth rate and therefore appears wider than the N-polar wing,[26] it is then possible to identify the *c*-direction which is along the Ga-polar growth front. Measurements of the widths for the Ga- and N-polar wing regions yield a ratio of approximately 2:1. This difference in growth rate between the two polarities has been attributed to differences in the adsorption and desorption rates[21] and the chemical stability of the two polarities[27] and growth temperature.

2.3 Current Leakage of ELO GaN Films

Current map images obtained using CAFM show distinct differences between the ELO samples (see Figs. 2.6 to 2.9). The lower quality L1 and L2 samples exhibit localized reverse-bias leakage in the window regions, whereas no such behavior is observed on the higher quality H1 and H2 samples. For sample L1, the most prominent features are leakage sites with currents up to 5 nA in the window regions and occasionally at meeting fronts (see Fig 2.6). The density of leakage sites in the windows is $\sim 2\times10^{7}$ cm^{-2}, which is comparable to densities previously reported for *c*-plane non-ELO GaN films.[28,29,30,31] Sample L2 exhibits a lower leakage site density of 1×10^{7} cm^{-2} with currents only up to 0.1 nA (see Fig 2.7). Since samples L1 and L2 both have leakage behavior in the window regions and also demonstrate the highest pit density and surface roughness in the windows, it is likely that surface pits are associated with dislocations[32] that exhibit high leakage current. This increased dislocation density may be related to growth conditions: sample L1 has a higher III/V ratio and previous studies suggest that Ga incorporation at screw dislocations is responsible for reverse-bias leakage at defect sites,[4,28,33] and sample L2 has Si doping that may increase current conduction. In addition to localized leakage behavior, some of the samples exhibit very low uniform current conduction in either the

wing regions (samples L2 and H1) or window regions (sample H1). This uniform current conduction does not appear to be correlated with any properties related to film quality. With regard to current conduction under forward-bias conditions, all four samples exhibited high resistance with no discernable turn-on voltage up to ~60 V. However, samples L1 and L2 showed forward-bias conduction at defect sites that demonstrated reverse-bias leakage. Figures 2.10(b) and 2.10(c) show reverse- and forward-bias current images, respectively, for sample L1 that indicate defect sites conduct in both biases.[34]

2.4 Conclusions

In summary, all four ELO samples showed the same general surface topography which consisted of striations along the *c*-direction and undulations due to depressions in the window regions. Window regions are visible in AFM images for samples grown via a two-step process due to the presence of surface pits that result in a higher surface roughness. Although some of the samples exhibited uniform conduction in either the window or wing regions, only the lower quality L1 and L2 samples demonstrated localized leakage in the window regions that could be detrimental to device performance.

Chapter 2 Figures

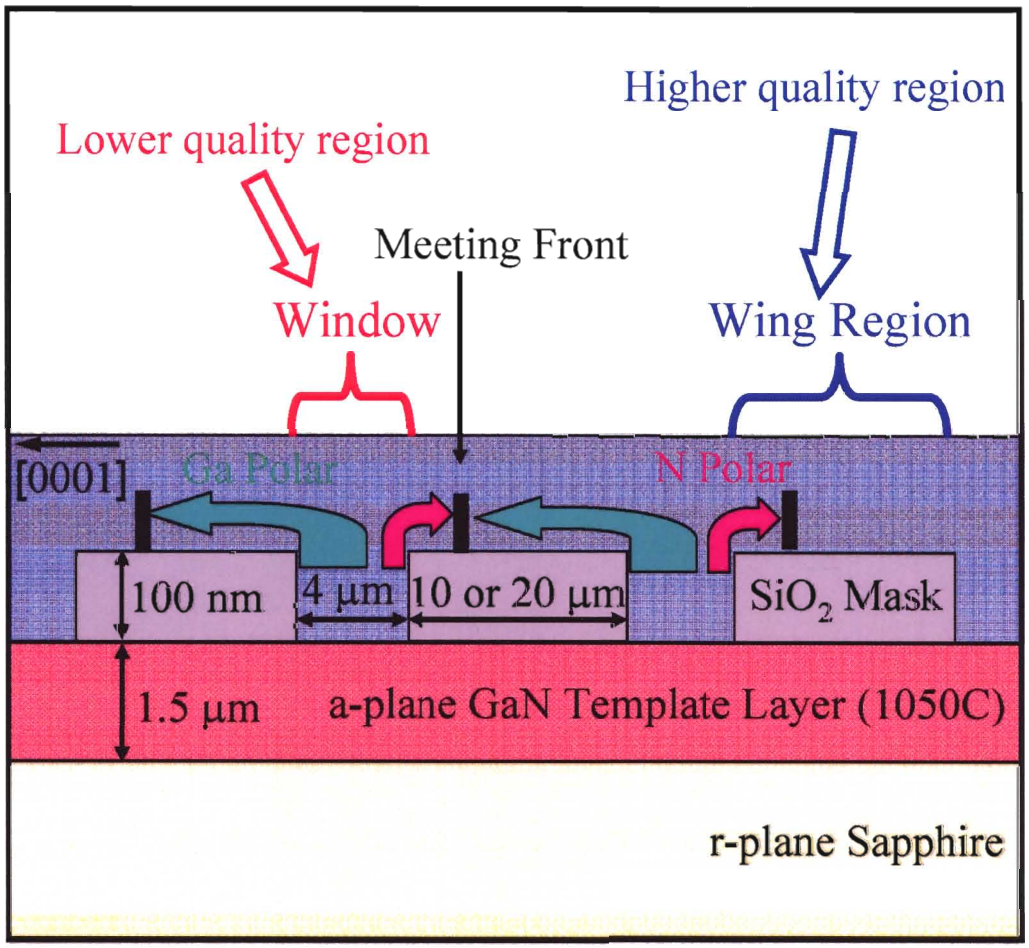

Fig 2.1: Side-view schematic of a sample grown using the method of epitaxial layer overgrowth (ELO).

Reference Sample #	**L1**		**L2**		**H1**		**H2**	
	Lower Quality				Higher Quality			
Growth Sample #	cvd1056-2 cvd1056sm cvd1056sm-2		cvd1242 cvd1242-2		cvd947		cvd1089-2	
	Stage I	Stage II	Stage I	Stage II	Stage I		Stage I	Stage II
Doping Level (cm^{-3})	0		$\sim 2\times10^{16}$		0		0	
TMG (μmol/min)	157	157	157	157	157		157	157
NH_3 (sccm)	3000	560	3000	3000	510		3000	3000
Growth Duration (h)	2.0	3.0	2.0	3.0	5.0		2.0	3.0
Temperature (°C)	1000	1050	1000	1050	1050		1000	1050
Region	Window	Wing	Window	Wing	Window	Wing	Window	Wing
Mean Roughness (nm)	5.6	3.9	2.3	1.6	22.6	16.5	1.6	1.4
Wing: Window Roughness Ratio	1.4		1.4		1.3		1.1	
Reverse-bias Leakage Site Density ($\times10^7$ cm^{-2})	2	-	1	-	-	-	-	-
TEM Threading Dislocation Density (Wing: Window) ($\times10^8$ cm^{-2}) *	-		-		1: 420		~ 1 :100	

Table 2.1: Growth and results data for ELO samples (*provided by the Morkoç group).

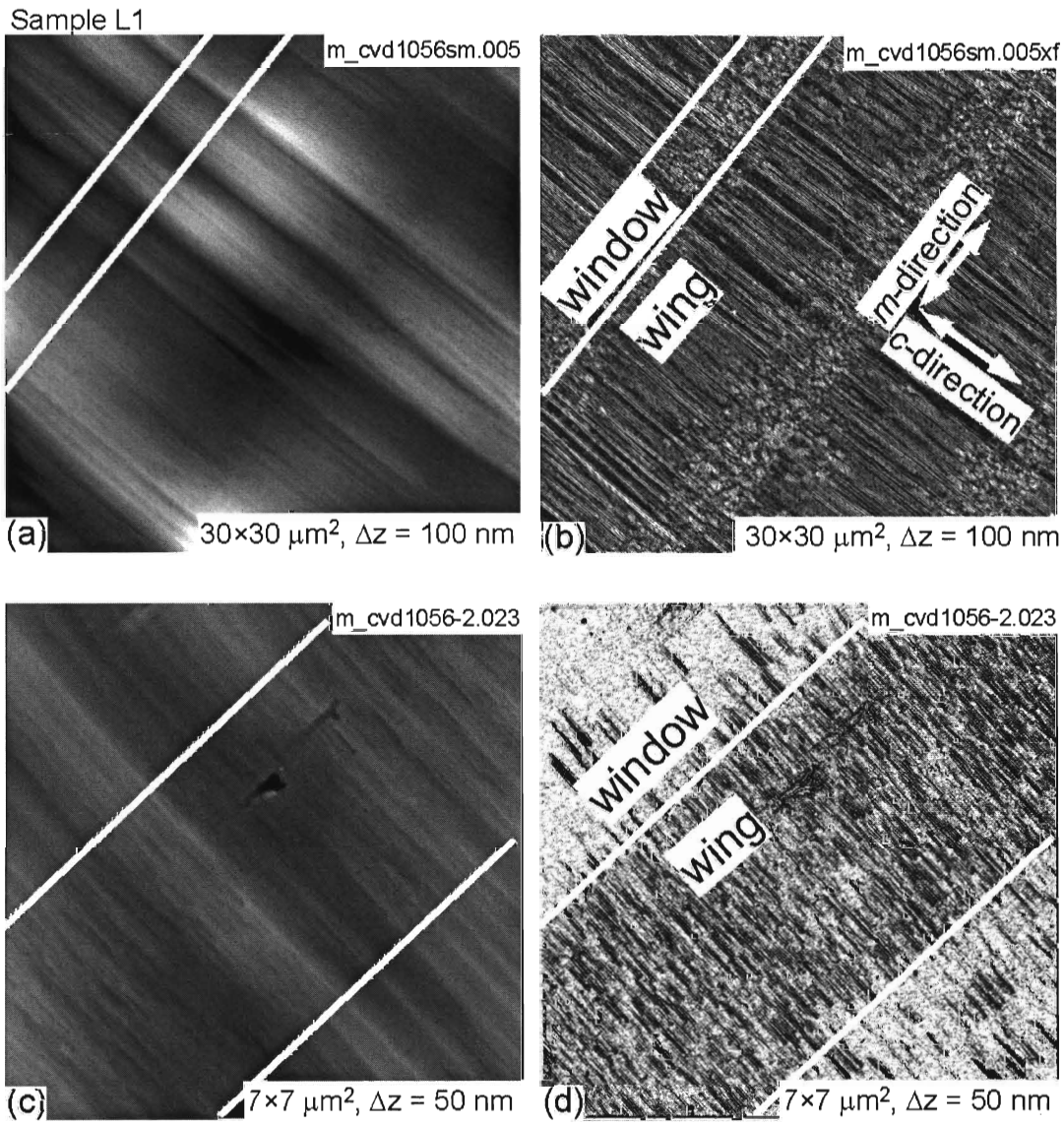

Fig 2.2: (a,c) Characteristic AFM topography images of sample L1 obtained using tapping-mode AFM and (b,d) images shown in (a,c) after Sobel processing for contrast enhancement. The pitch of the ELO pattern is 14 μm in (a,b) and 24 μm in (c,d).

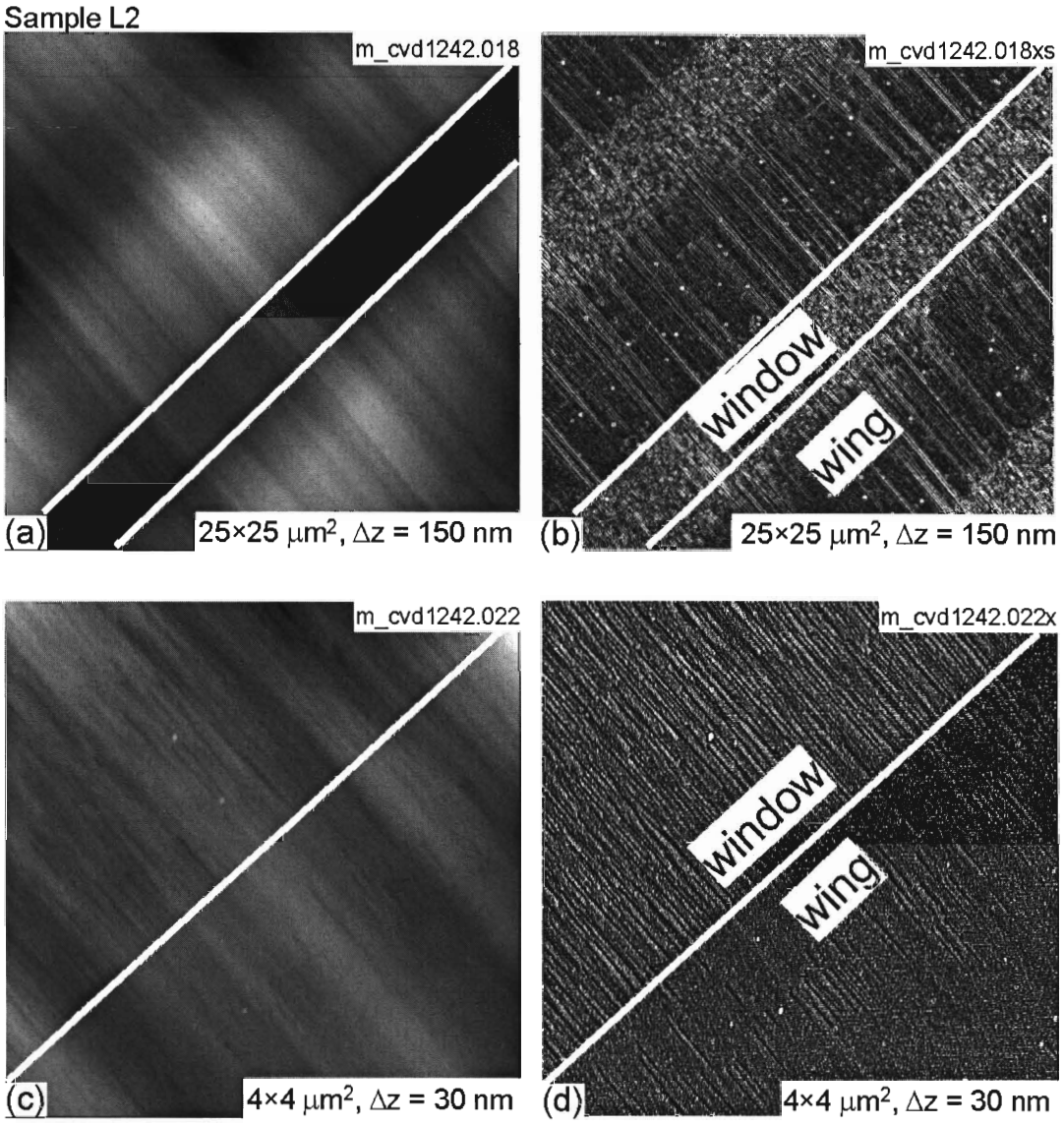

Fig 2.3: (a,c) Characteristic AFM topography images of sample L2 obtained using tapping-mode AFM and (b,d) images shown in (a,c) after Sobel processing for contrast enhancement. The pitch of the ELO pattern is 14 μm.

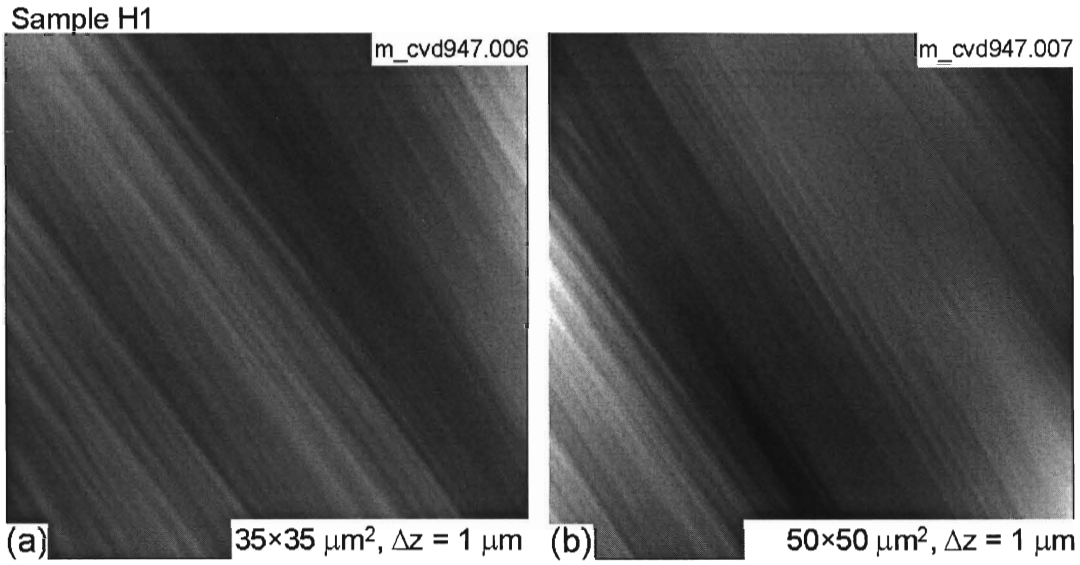

Fig 2.4: Characteristic AFM topography images of sample H1 obtained using tapping-mode AFM. The pitch of the ELO pattern is 24 μm.

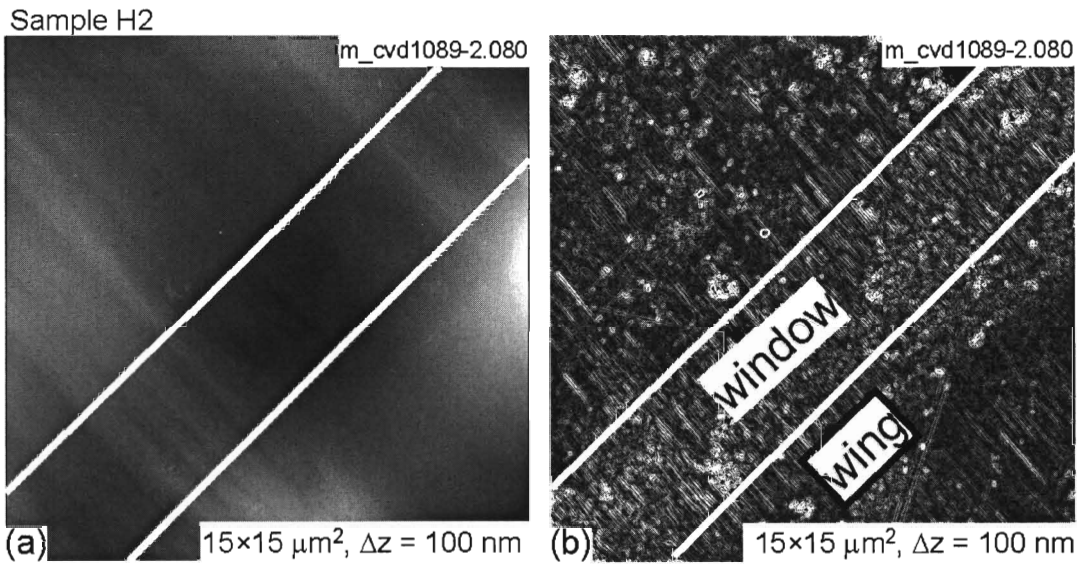

Fig 2.5: (a) Characteristic AFM topography image of sample H2 obtained using tapping-mode AFM and (b) image shown in (a) after Sobel processing for contrast enhancement. The pitch of the ELO pattern is 14 μm.

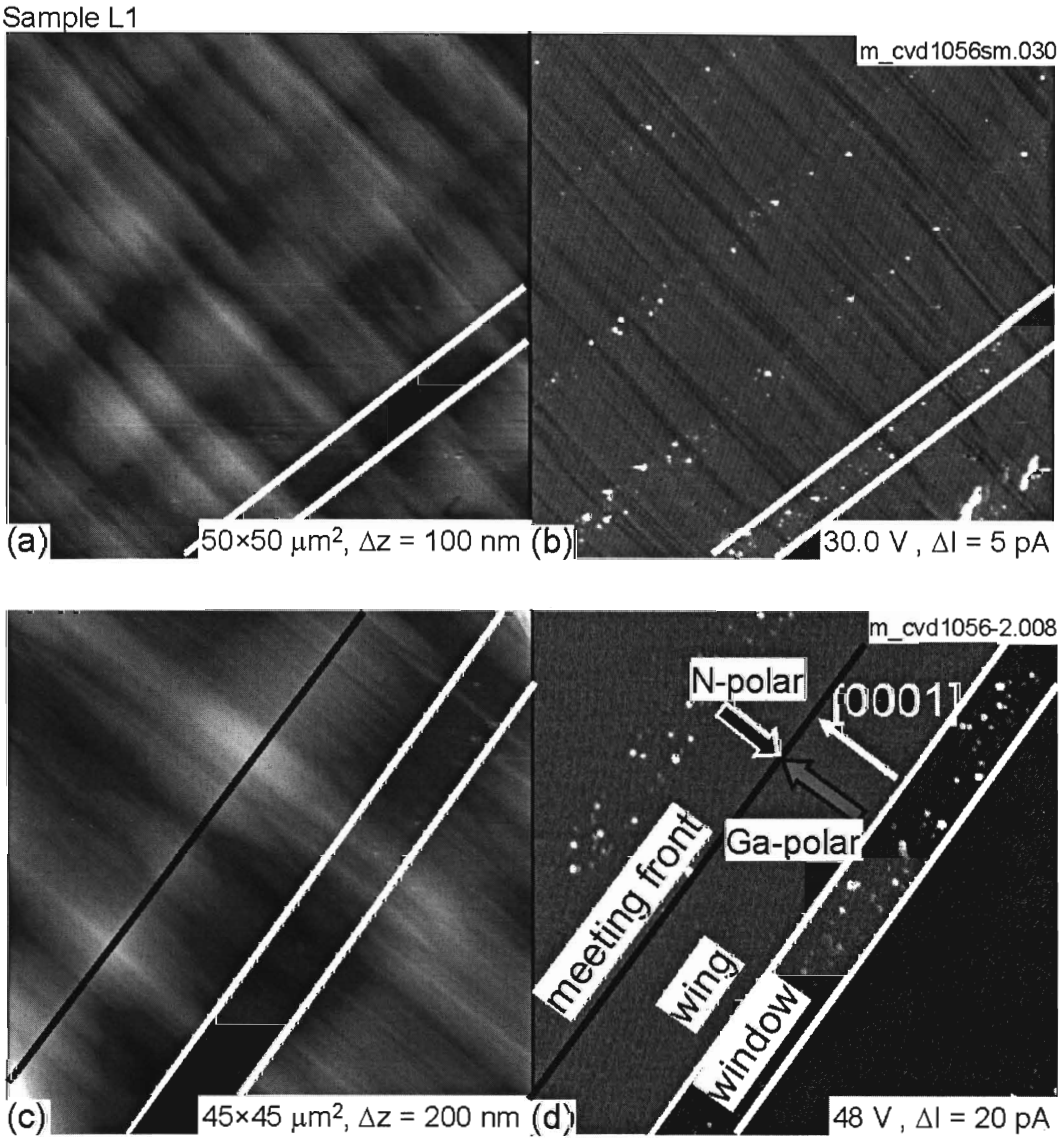

Fig 2.6: (a,c) Characteristic AFM topography images of sample L1 obtained using contact-mode AFM and (b,d) simultaneous current images obtained using the TUNA module. The pitch of the ELO pattern is 14 μm in (a,b) and 24 μm in (c,d).

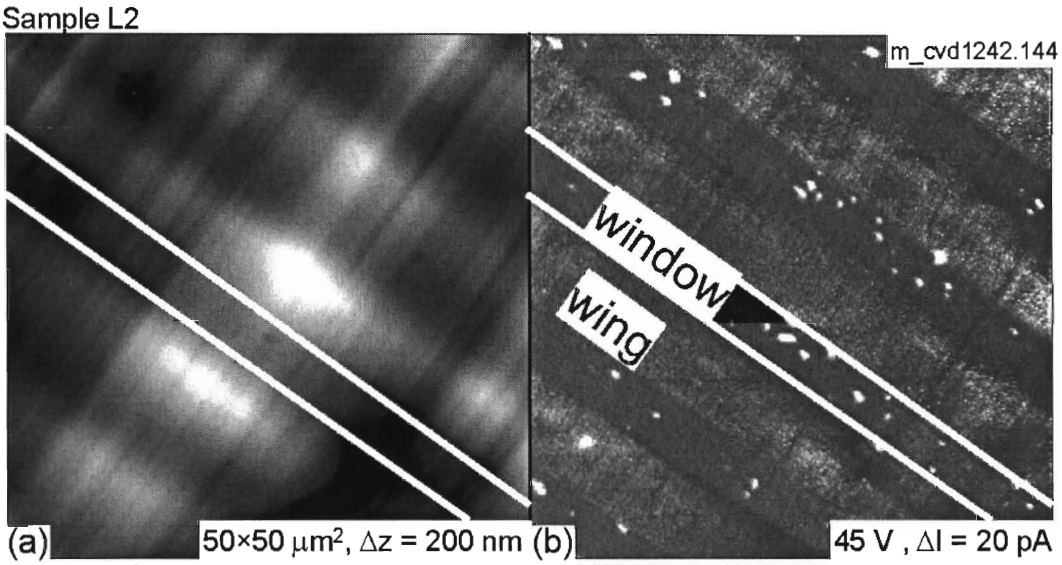

Fig 2.7: (a) Characteristic AFM topography image of sample L2 obtained using contact-mode AFM and (b) simultaneous current images obtained using the TUNA module. The pitch of the ELO pattern is 14 μm.

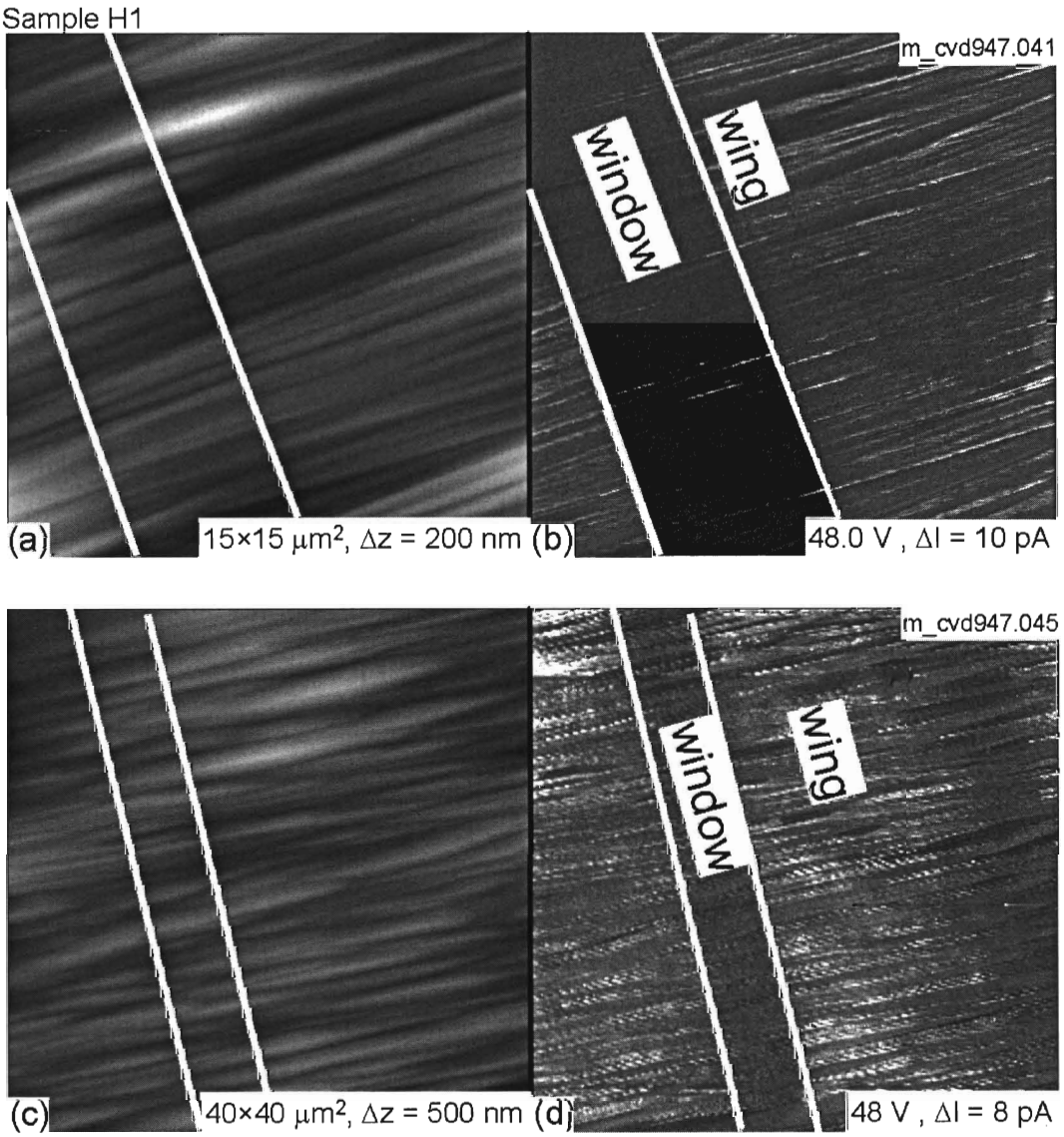

Fig 2.8: (a,c) Characteristic AFM topography images of sample H1 obtained using contact-mode AFM and (b,d) simultaneous current images obtained using the TUNA module. The pitch of the ELO pattern is 24 μm.

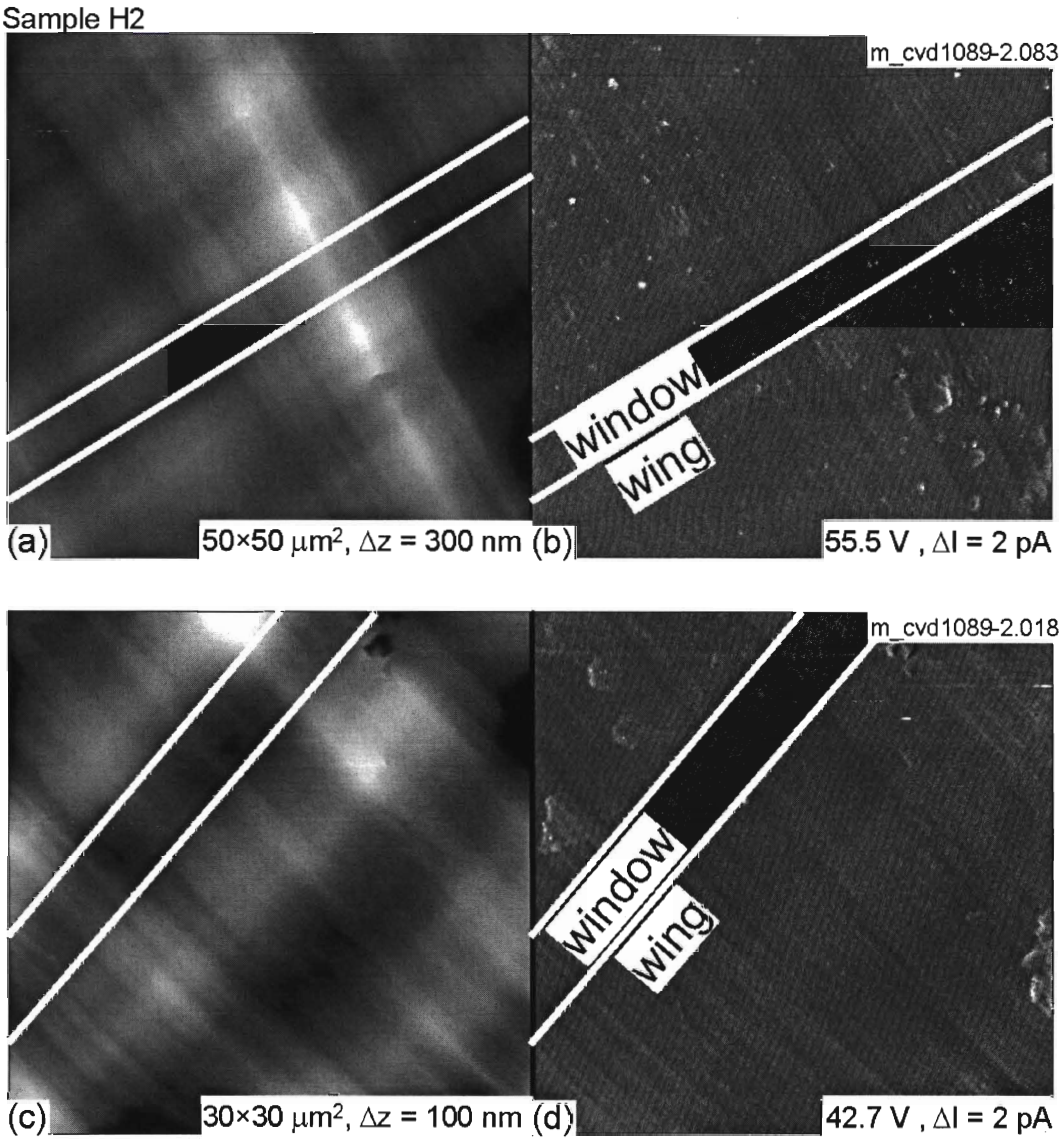

Fig 2.9: (a,c) Characteristic AFM topography images of sample H2 obtained using contact-mode AFM and (b,d) simultaneous current images obtained using the TUNA module. The pitch of the ELO pattern is 14 μm.

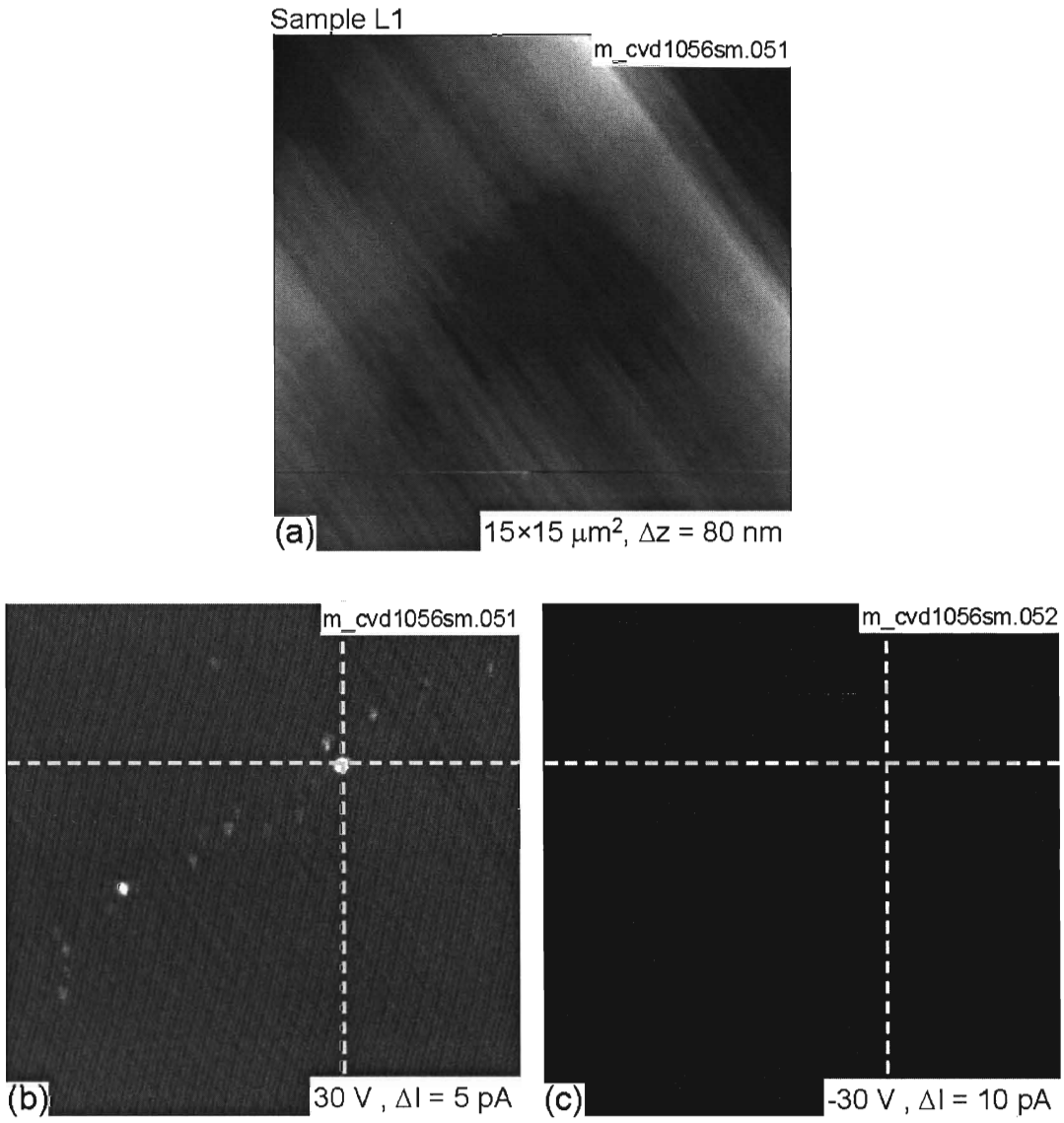

Fig 2.10: (a) L1 topography taken using contact-mode AFM and (b) simultaneous current image taken using the TUNA module showing leakage sites in the window regions. (c) Current image taken subsequently under forward-bias.

Chapter 3: Nano-ELO

3.1 Introduction

The use of the ELO technique discussed in the previous chapter has a major disadvantage because it requires an *ex situ* photolithography and etching step. This causes an interruption in growth and can lead to sample contamination and impurity incorporation. An alternative to the ELO technique is a "nano-ELO" technique that uses an *in situ* nano-network formed by a silicon nitride (Si_3N_4) layer. This layer can be deposited on a GaN template by replacing the trimethyl gallium gas [TMG, $Ga(CH_3)_3$] used during MOCVD growth with silane [SiH_4] diluted by hydrogen. By controlling the flow rate, concentration, and deposition time of the silane, it is possible to achieve a porous morphology in the final Si_3N_4 layer. Subsequent GaN overgrowth begins via the formation of GaN seeds in the open pores of the Si_3N_4 layer followed by the growth of these seeds through the nano-network. The nano-ELO process using Si_3N_4 was first developed in the late nineties when studying the effects of Si_3N_4 treatment on sapphire[35] and standard ELO growth using Si_3N_4.[36] The first demonstration of nano-ELO during MOCVD GaN film growth was reported in 2000.[37,38] Reductions in threading dislocation densities have been reported,[39,40] along with favorable results for photodetector[41] and multiple quantum well (MQW) LED devices.[42] Schottky diodes fabricated on nano-ELO GaN have also been studied.[40]

In this study, five nano-ELO samples grown in the Morkoc research group were examined. GaN templates were prepared by growing *c*-plane GaN using MOCVD on *c*-plane sapphire substrates (see Fig 3.1). The Si_3N_4 layer was then deposited on the GaN template by flowing 50 sccm of 100 ppm silane (SiH_4) diluted in H_2.[43] Since previous studies of nano-ELO on 6H SiC substrates[44] have suggested studying the thickness dependence of the Si_3N_4 nano-net, the Si_3N_4 deposition time was varied between samples. The GaN overgrowth layer was deposited at 1040 °C until coalescence occurred (see Table 3.1 for details), and then a 500 nm–thick top layer was grown with Si-doping (1.5×10^{17} cm^{-3}) to increase sample conductivity.[43] The samples were prepared with 0, 4, 5, 6 and 10 min of Si_3N_4 deposition time and will be referred to in this study

as 0M, 4M, 5M, 6M, and 5+5M, respectively. Sample 0M had no Si_3N_4 layer and serves as a control, and sample 5+5M had two sequential 5 min. Si_3N_4 growth runs.

3.2 Topography of Nano-ELO GaN Films

All five nano-ELO samples grown using the Si_3N_4 nano-network demonstrated similar topographies with an ordered step-plus-terrace morphology (see Figs. 3.2 and 3.3). Samples 0M, 5M and 5+5M displayed similar terrace lengths (170 nm), while sample 6M had narrower terraces (110 nm). In some cases, surface pits (90–120 nm dia.; 1–2 nm deep) were also observed on the samples. Samples 0M and 5M had no surface pits (see Fig. 3.2), although scratches can be seen on sample 5M. Samples 6M and 5+5M displayed moderate densities of surface pits, 4×10^7 cm^{-2} and 8×10^7 cm^{-2}, respectively, with step bunching at the sites of these surface pits (see Fig. 3.3). Sample 4M displayed the highest pit density (22×10^7 cm^{-2}) and had a distinctively different surface morphology as a result [see Fig. 3.3(e) and 3.3(f)]. Table 3.1 also presents the density of threading dislocations as determined by TEM measurements for the samples. There is a reasonable correlation between the density of threading dislocations and the density of surface pits, indicating that pits may indicate the termination sites of dislocations.

3.3 Current Leakage of Nano-ELO GaN Films

Reverse-bias CAFM measurements were performed on all samples at voltages up to 56 V, with most samples demonstrating a low density of localized leakage defects. Typical current map images for the different samples are shown in Figs. 3.4 to 3.7. Localized leakage sites are indicated on the current images with circles. The densities of these leakage sites at 56 V were calculated and this information, along with typical maximum observed leakage current values, is presented in Table 3.1. Leakage site densities range from 0.8×10^6 cm^{-2} for sample 4M to 4.6×10^6 cm^{-2} for sample 0M. The densities of leakage sites are two orders of magnitude lower than the densities of threading dislocations observed with TEM on samples 4M and 6M, suggesting that a majority of the dislocations do not contribute to reverse-bias leakage. Sample 4M exhibited the largest reverse-bias leakage currents (~5.6 nA), but the density of leakage sites (~0.8×10^6 cm^{-2}) is comparable with the other samples. No leakage sites were observed on a total area of 800 μm^2

on sample 5+5M at a reverse-bias voltage of 56 V, indicating that the density of leakage sites is lower than 1×10^6 cm^{-2}. However, a leakage spot was observed in one series of lower voltage scans. Figure 3.7 shows the presence of a leakage site (initial leakage current ~ 1.2 nA) during the first scan [Fig. 3.7(b)] and the subsequent growth of an oxide protrusion and leakage cutoff for subsequent scans [Figs. 3.7(c) and 3.7(d)]. The application of a higher voltage caused the leakage site (0.9 nA) to reappear [see Fig 3.7(f)]. Therefore, while an estimate of the density of reverse-bias leakage sites could not be obtained on sample 5+5M, isolated leakage sites can be found.

3.4 Conclusions

Samples grown via nano-ELO techniques with a Si_3N_4 nano-net exhibit a flat topography with terraces. The presence of threading dislocations manifests itself in the form of surface pits. High-voltage CAFM studies indicate that a majority of the threading dislocations present in the sample do not result in the presence of reverse-bias leakage sites on the sample surface. Both samples 4M and 6M exhibit nearly identical densities (0.8×10^6 cm^{-2} and 1.0×10^6 cm^{-2}) of leakage sites, while sample 5+5M appears to have the lowest density of leakage sites ($<1\times10^6$ cm^{-2}), indicating that while the density of these sites may not be directly correlated with Si_3N_4 nano-net deposition time, the use of a two-step nano-ELO process results in fewer leakage sites. Based on current statistics, nano-ELO GaN thin film samples therefore appear to be very promising candidates for the growth of high quality films for device applications.

Chapter 3 Figures

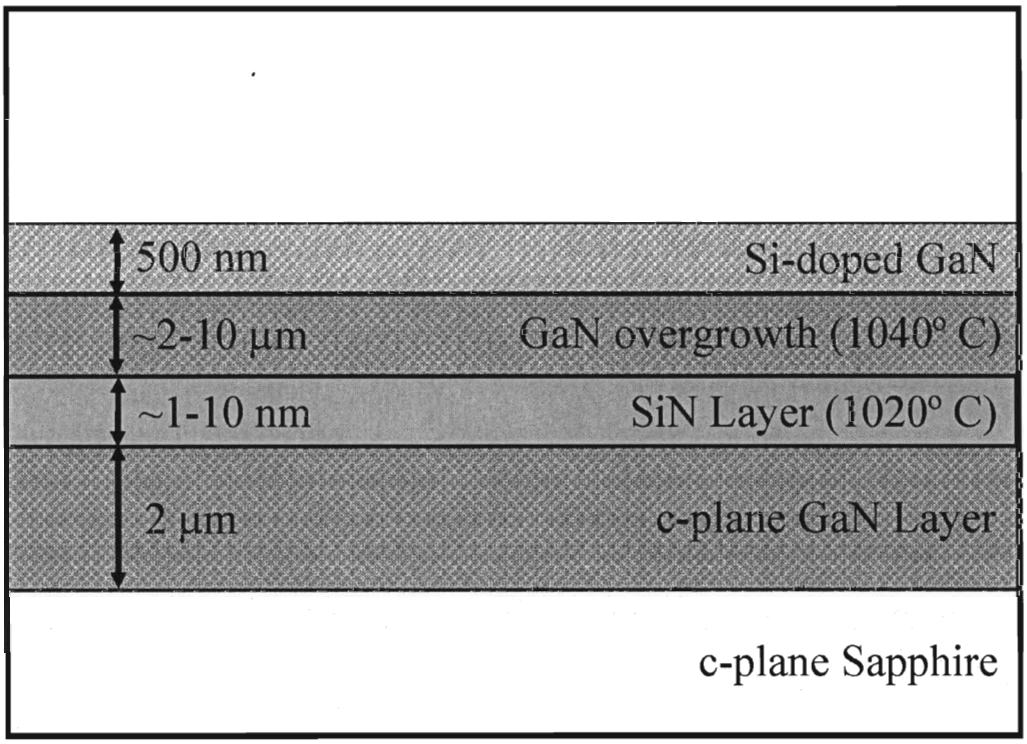

Fig 3.1: Side-view schematic of nano-ELO samples.

Reference Sample #	0M	4M	5M	6M	5+5M
Growth Sample #	cvd1099d 1129	cvd1099	cvd1236	cvd1090-2	cvd1216c-2
Si_3N_4 growth time (min)	0	4	5	6	5+5
SiH_4 (sccm @ 100 ppm)	50				
Doping level (cm^{-3})	$\sim 1.5\times10^{17}$				
TMG (μmol/min)	80				
V/III Ratio	4000				
TEM threading dislocation density ($\times10^8$ cm^{-2})*	-	5	1	0.5	< 1
Density of surface pits ($\times10^8$ cm^{-2})	-	2.2	-	0.4	0.8
Terrace length (nm)	170	150	170	110	170
Density of reverse-bias leakage sites ($\times10^6$ cm^{-2})	4.6	0.8	-	1.0	< 1
No.of leakage sites / Area (μm^{-2})	32/700	5/600	-	6/600	0/800
Max. currents at leakage sites at 56V (pA)	80	5600	-	50	-

Table 3.1: Growth and results data for nano-ELO samples (*provided by Morkoç group).

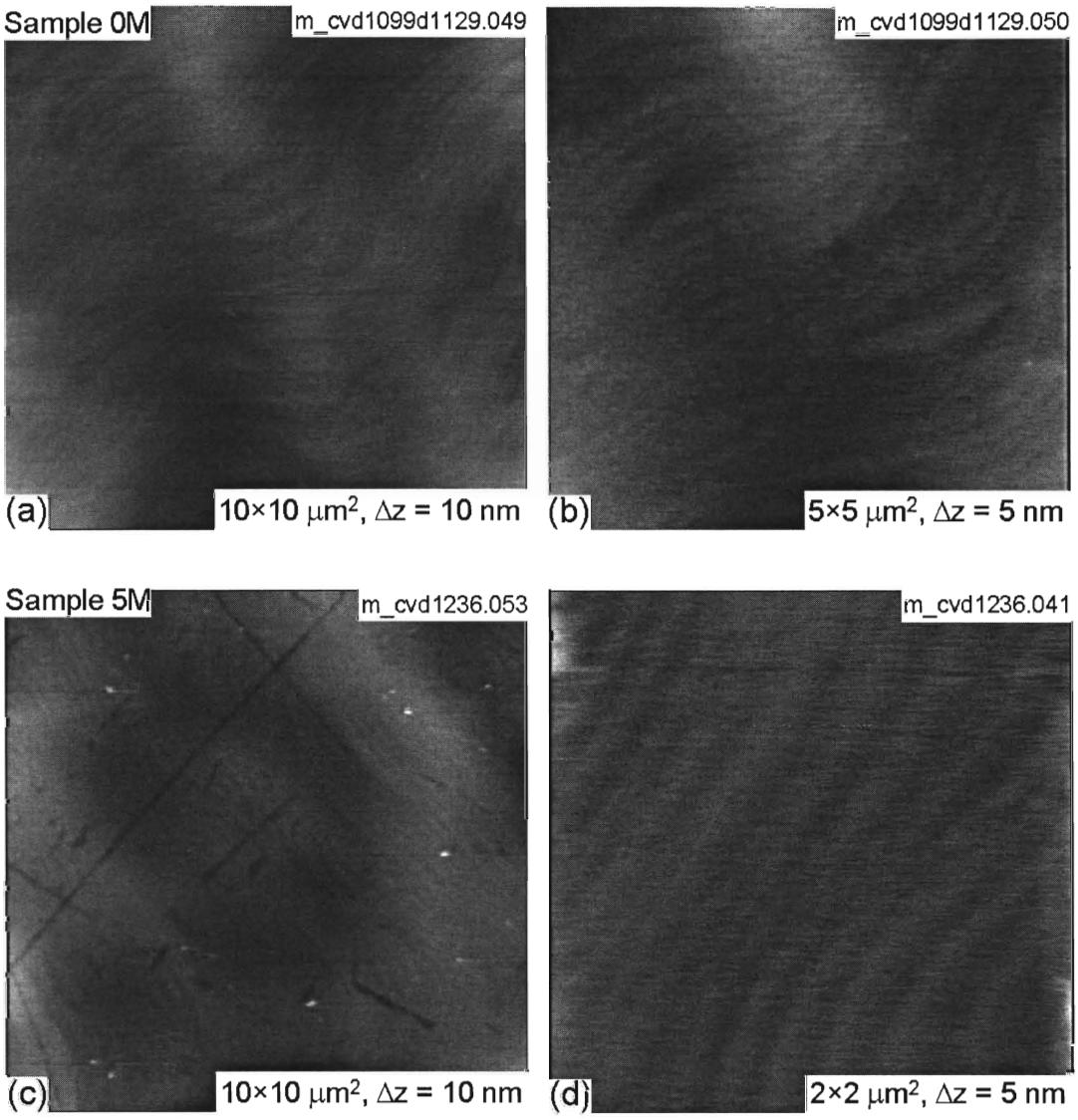

Fig 3.2: Characteristic AFM topography images obtained using contact-mode AFM of (a,b) sample 0M and (c,d) sample 5M.

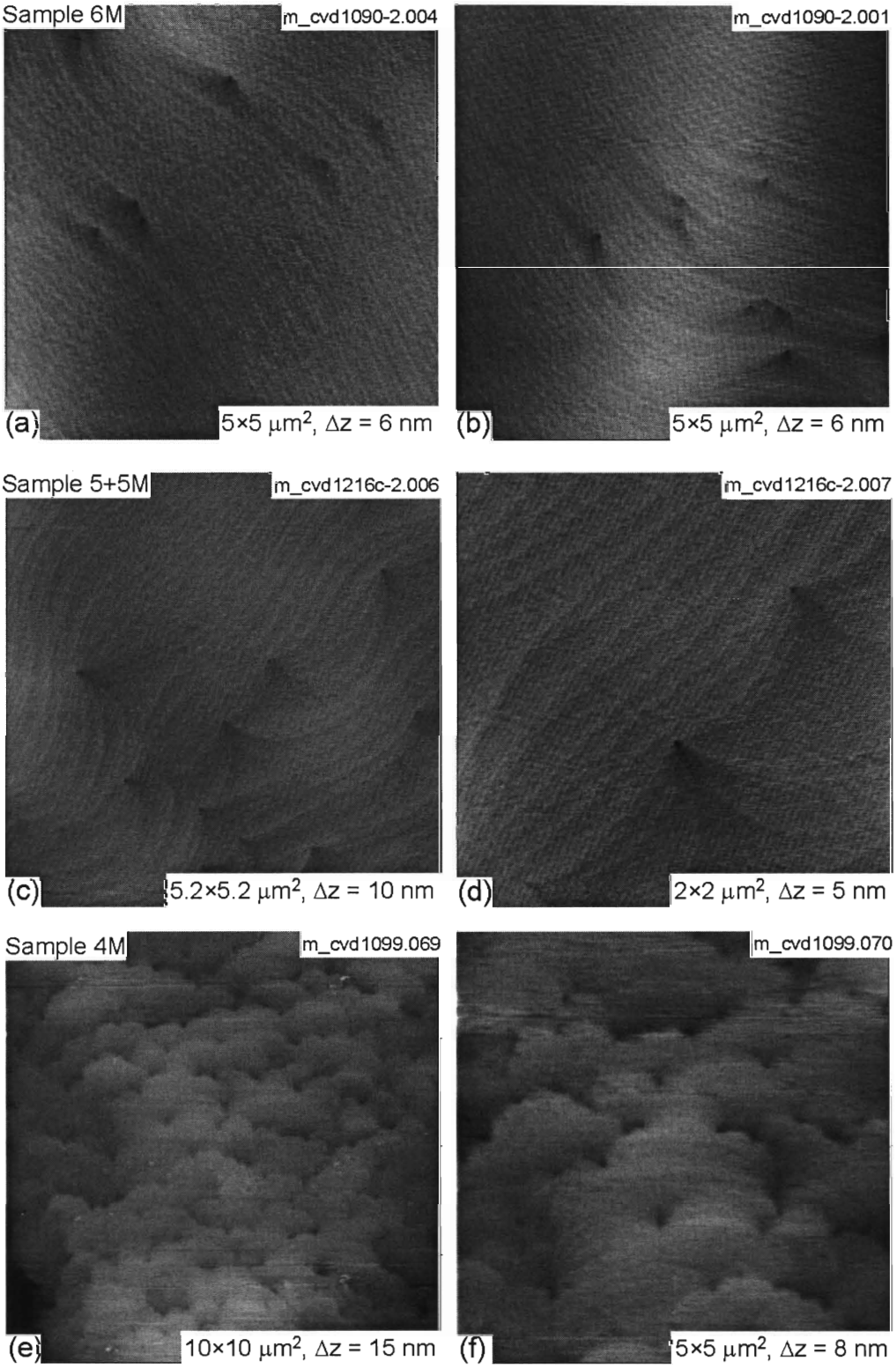

Fig 3.3: Characteristic AFM topography images of (a, b) sample 6M, (c, d) sample 5+5M obtained using tapping-mode AFM and (e, f) sample 4M obtained using contact-mode AFM.

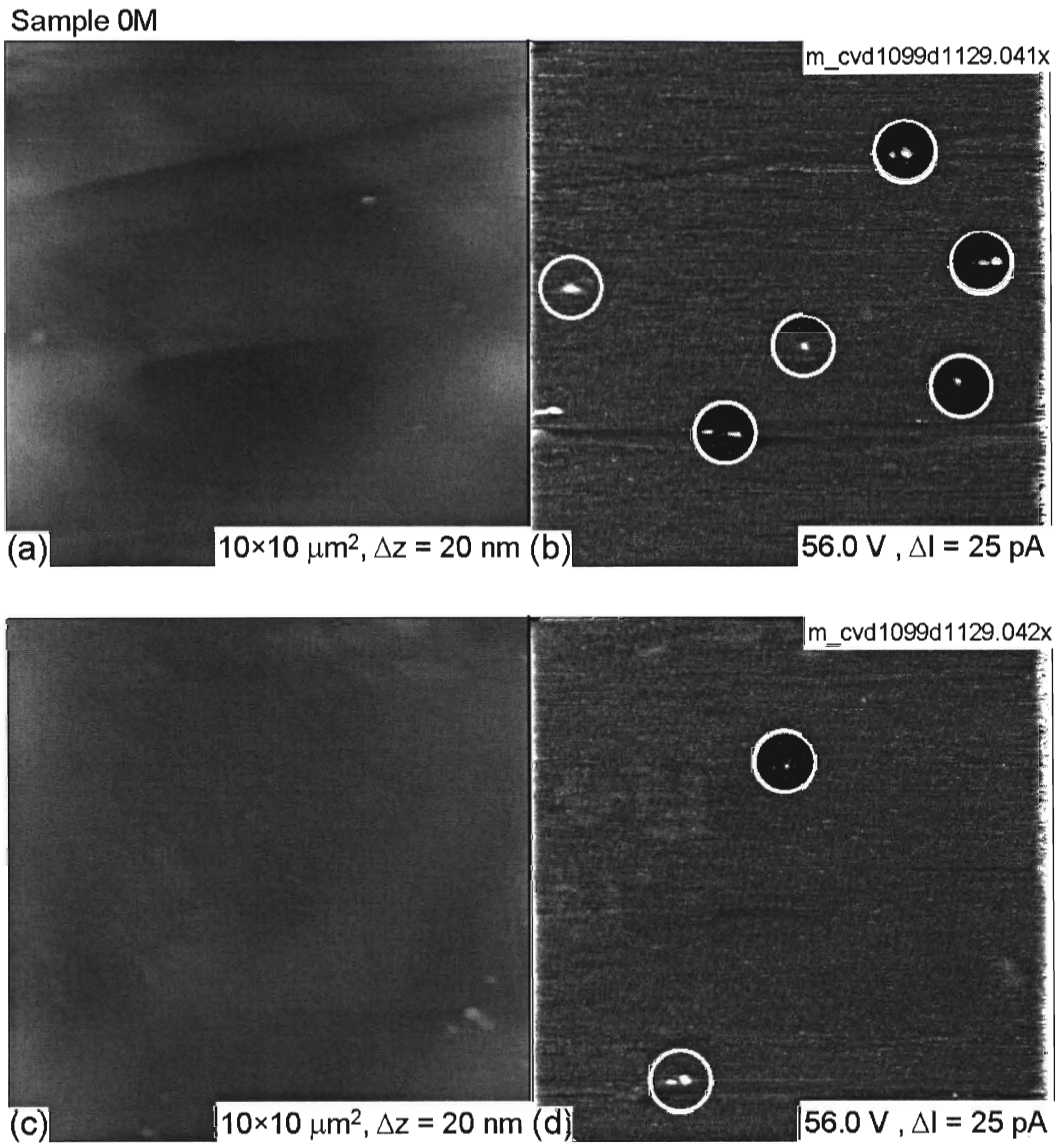

Fig 3.4: (a,c) Characteristic AFM topography images of sample 0M obtained using contact-mode AFM and (b,d) simultaneous current images obtained using the CAFM module.

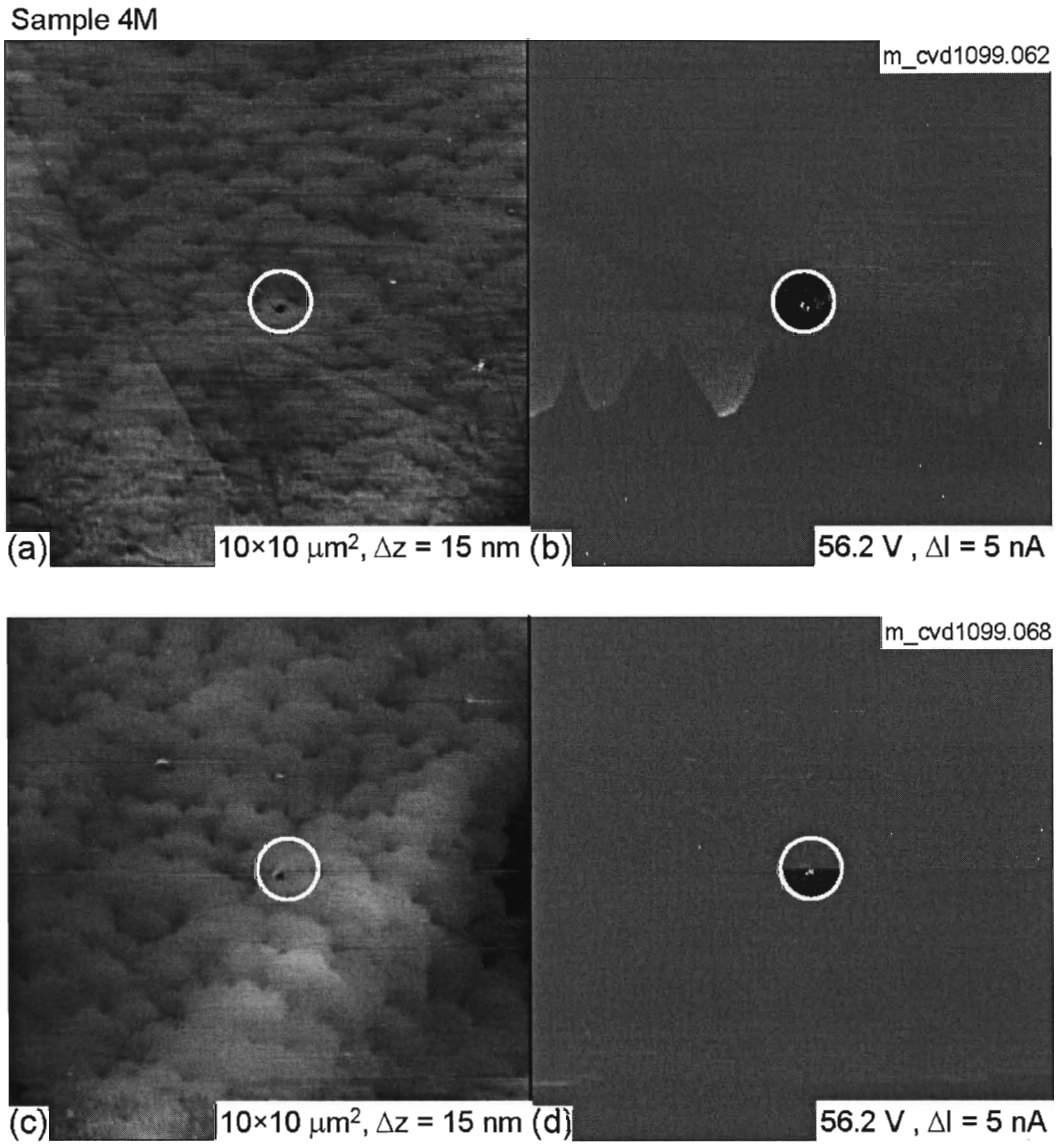

Fig 3.5: (a,c) Characteristic AFM topography images of sample 4M obtained using contact-mode AFM and (b,d) simultaneous current images obtained using the CAFM module.

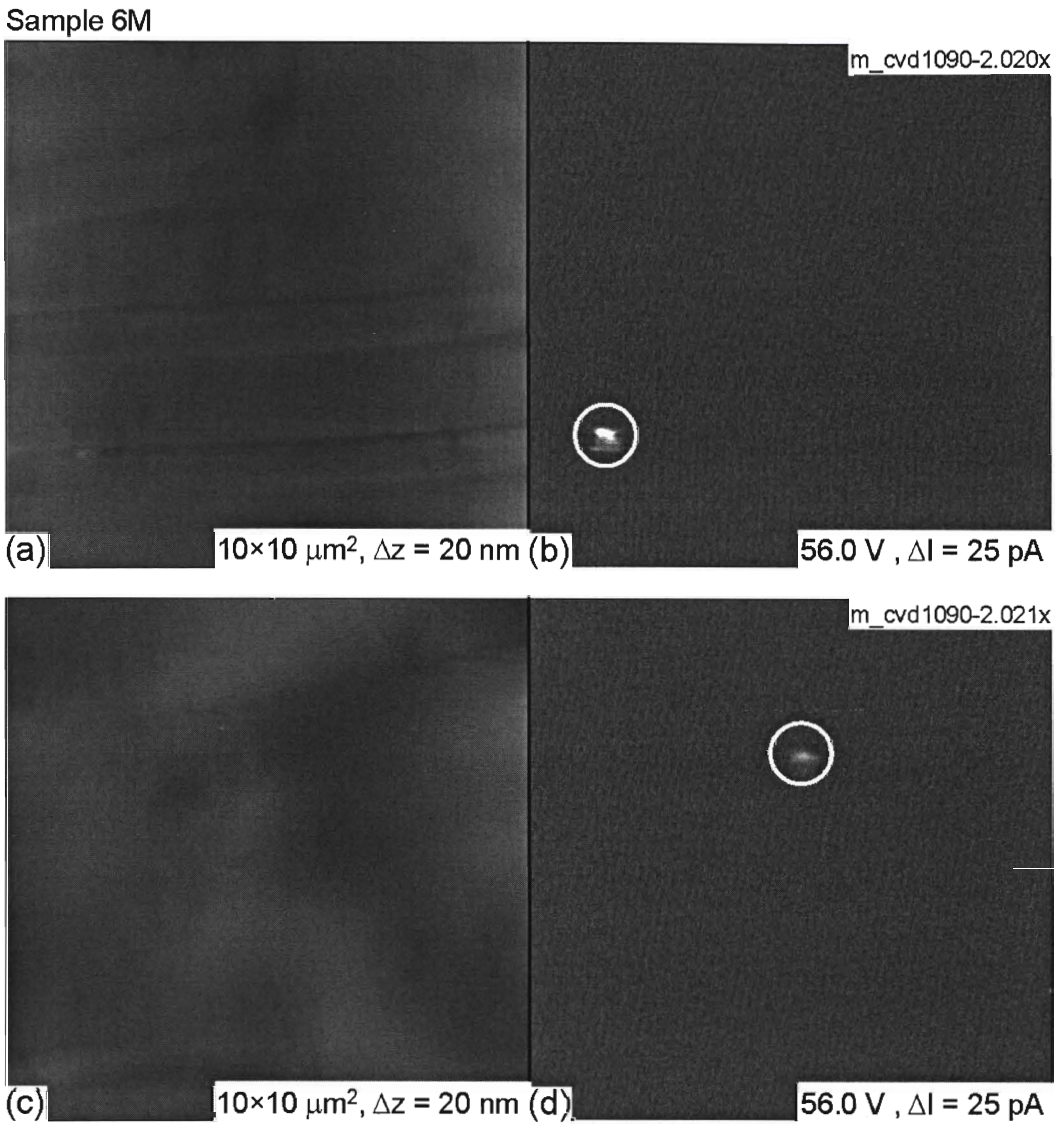

Fig 3.6: (a,c) Characteristic AFM topography images of sample 6M obtained using contact-mode AFM and (b,d) simultaneous current images obtained using the CAFM module.

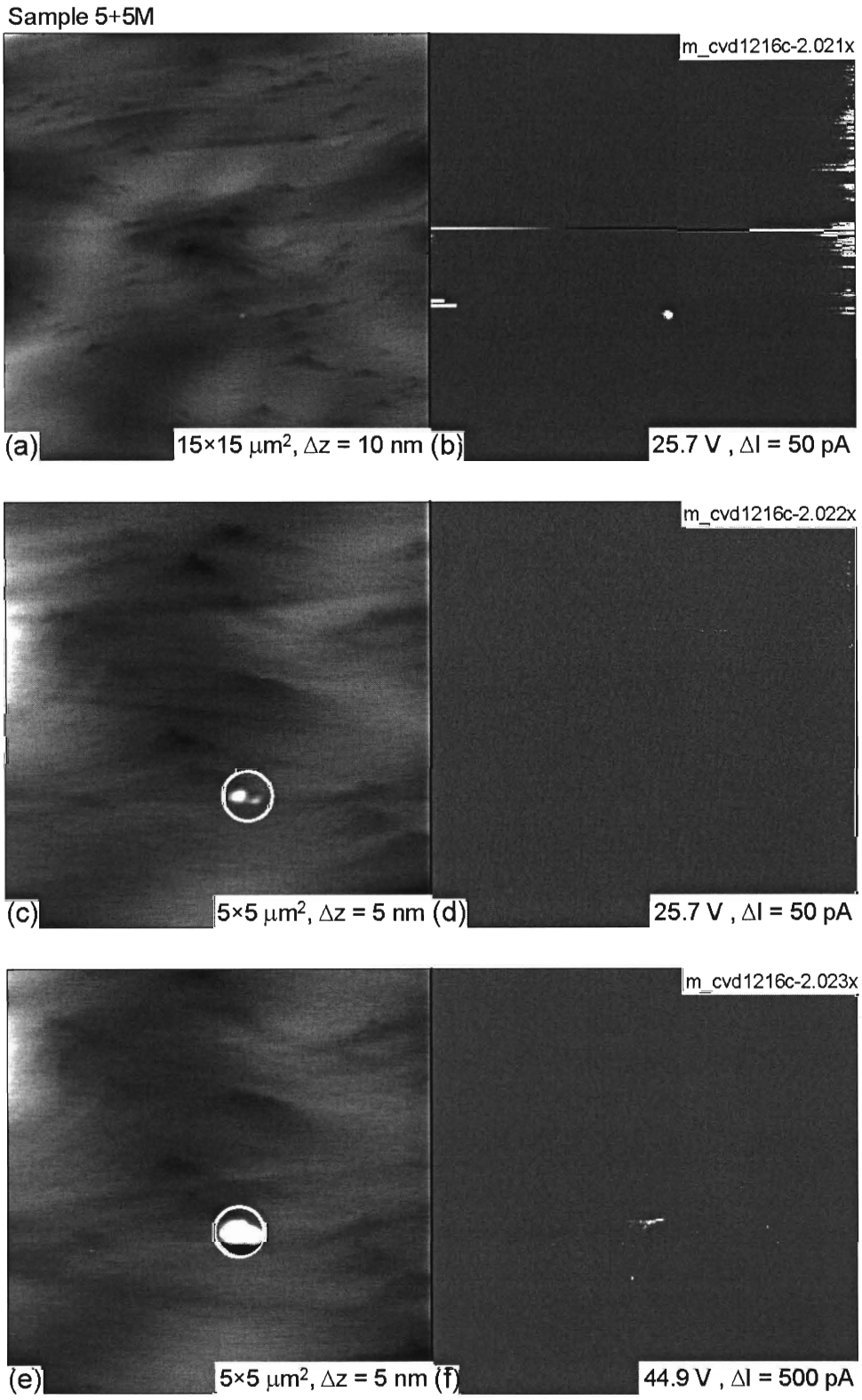

Fig 3.7: (a,c,e) Characteristic AFM topography images of sample 5+5M obtained using contact-mode AFM and (b,d,f) simultaneous current images obtained using the CAFM module showing oxide growth.

Chapter 4: Conclusions

4.1 Introduction

CAFM studies have been performed for samples grown using both ELO and nano-ELO techniques. A few observed behaviors that hindered these studies will be briefly discussed here for completeness. Finally, a discussion is presented of ELO vs. nano-ELO growth techniques from the viewpoint of device fabrication based on the observed reverse-bias performance.

4.2 Oxide Growth

All of the samples in this study displayed possible oxide growth while performing reverse-bias CAFM. Figure 4.1 shows topography and current images acquired on ELO sample H1 that demonstrate this behavior. The region seen in the square box of low conductance in the top right-hand corner of Fig. 4.1(b) was scanned several times before zooming out for data acquisition. The repeated scanning appears to result in the growth of a thin layer of surface oxide that decreases current conduction. This effect is seen more prominently in Fig. 4.2 for a doped MOCVD GaN template layer similar to sample 0M. After repeated scanning in a smaller region [Fig. 4.2(a) and 4.2(b)], a larger-scale CAFM image is acquired [Fig. 4.2(c) and 4.2(d)] where a boxed region with higher topography due to oxide growth corresponds to a boxed region of lowered conductance. Such oxide growth has previously been suggested as the cause for the formation of protrusions at leakage sites on MBE GaN films.[45] Similar protrusions were observed in this study (see Fig 3.7), which lead to difficulties in accurately measuring reverse-bias leakage current at defect sites if the site has already been scanned. Hence, all images used in this study to determine the densities of localized leakage sites were obtained at new locations. It should also be noted that oxide growth may also occasionally result in charging behavior. For example, oxide growth is seen at the circled defect site in the first scan in Fig 4.3(a). Subsequently, the protrusion in AFM data appears as a depression [Fig 4.3(c)], possibly caused by charging at the defect followed by a Coulomb interaction between the tip and sample.

4.3 Surface Contamination Films

For the nano-ELO study, CAFM data could not be obtained on samples 5M, as well as parts of 6M and 5+5M. This behavior could be due to the presence of an insulating layer of unknown composition. This surface layer could only occasionally be removed by repeated scanning of the surface in contact mode followed by CAFM imaging [see Fig. 4.4] The region of lower conductance seen in Fig. 4.4(b) appears as a region of increased conductance in Fig. 4.4(d). This effect of removing a surface layer is vividly demonstrated in Fig. 4.5, where the boxed region in the center of Fig. 4.5(a) was created by repeatedly scanning a 2×2 μm^2 box. The exact sequence of scans is listed in Table 4.2. Similar layers may have existed on samples 6M and 5+5M, making it impossible to obtain CAFM data on these samples. The presence of a surface layer on samples as shown here suggests that care must be taken when interpreting data.

4.4 ELO vs. Nano-ELO

The ELO and nano-ELO techniques are both growth techniques developed to address the same concern – reducing the density of defects in epitaxial GaN so that it is suitable for device fabrication. The presence of defects that exhibit large reverse-bias leakage currents would inhibit the performance of any type of rectifier device. Both ELO and nano-ELO show promise in reducing such defects. The two techniques would however have different applications. Recall that ELO samples H1 and H2 exhibited no leakage sites, whereas samples L1 and L2 exhibited leakage sites but only in the window regions. Hence, device fabrication with no detectable leakage is possible on all of the ELO samples over the wing regions. Disadvantages to note are that the device is restricted to the wing width and rigorous care must be taken while patterning the ELO template to avoid contamination. The nano-ELO samples had an overall lower density of leakage sites ($\sim10^6$ cm^{-2}) as compared to standard *c*-plane GaN films ($\sim10^7$ cm^{-2}).[28] Sample 5+5M displayed only one leakage site, but this growth condition required two Si_3N_4 layers, making it inherently more time-consuming to produce since coalescence must be achieved twice. Therefore, when the tolerance level for leakage sites is very low, ELO growth may be used provided that the device size is sufficiently small to fit within the wing regions. Since the nano-ELO process is *in situ*, it may be used when production costs are a more pressing concern.

Chapter 4 Figures

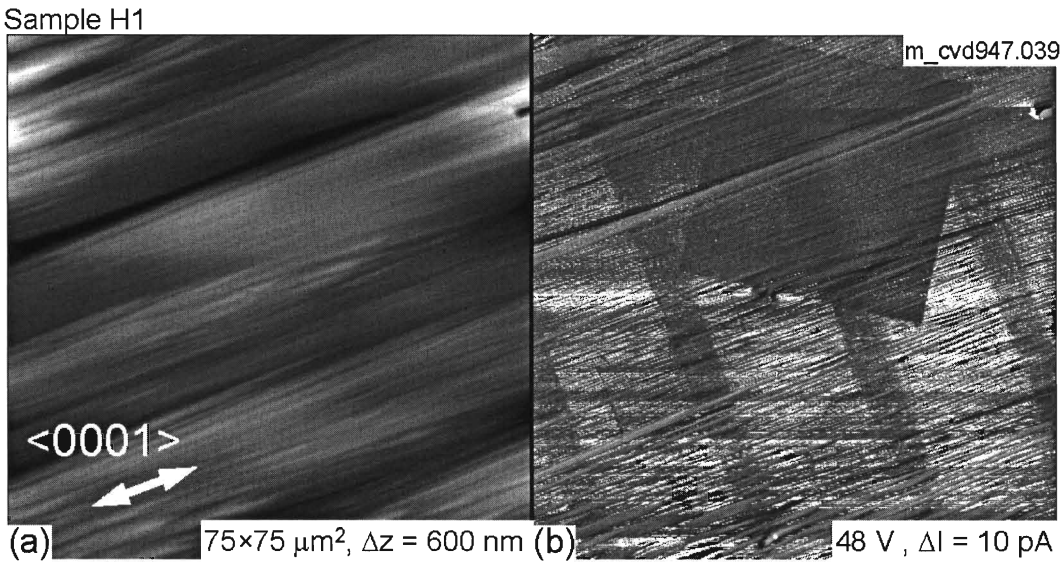

Fig 4.1: (a) Sample H1 topography taken using contact-mode AFM and (b) simultaneous current image taken using the TUNA module showing a boxed region of lowered conduction created by previous scans.

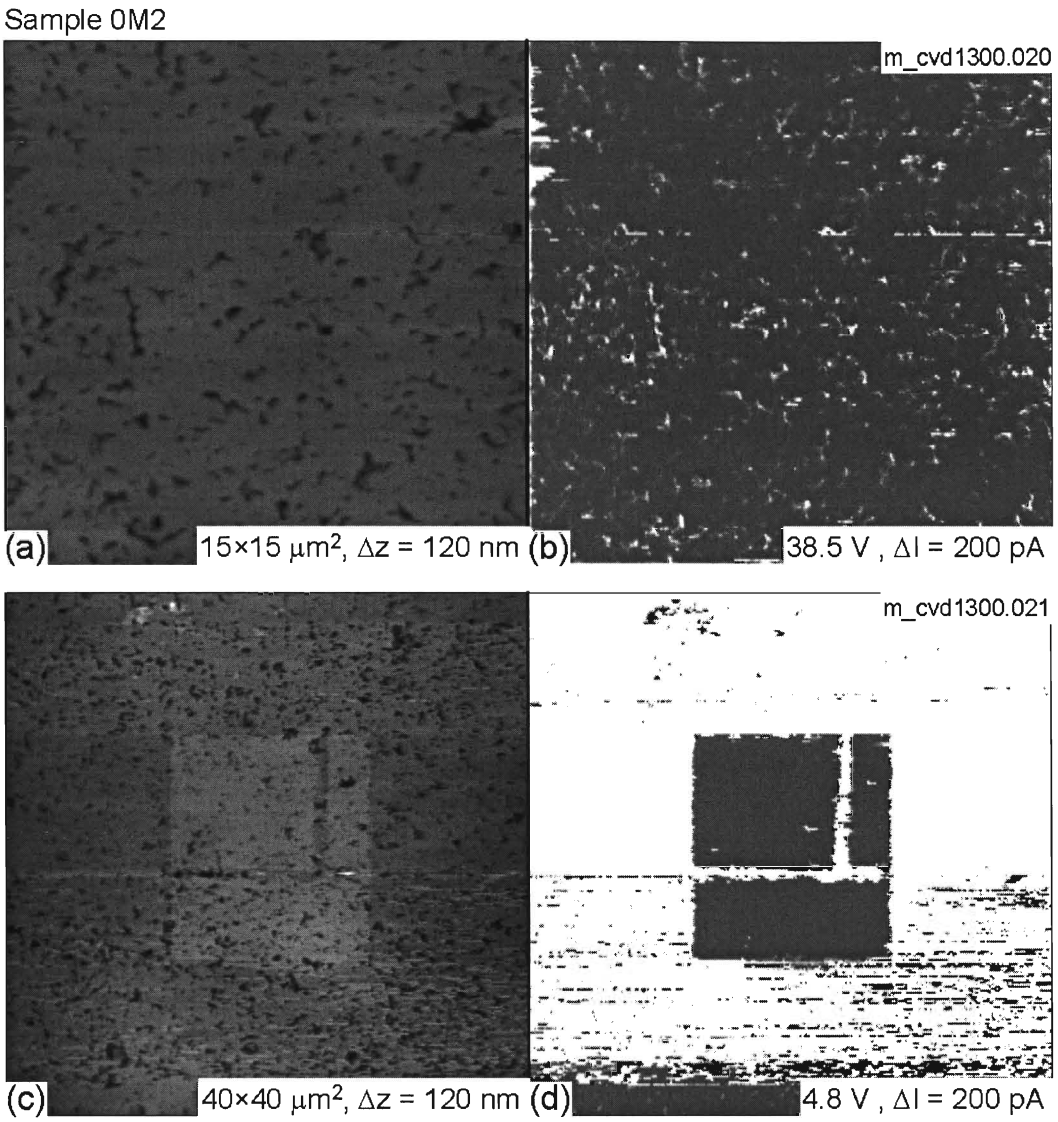

Fig 4.2: (a,c) Topography taken using contact-mode AFM and (b,d) simultaneous current images taken using the C-AFM module showing a boxed region of lowered conduction created by previous scans.

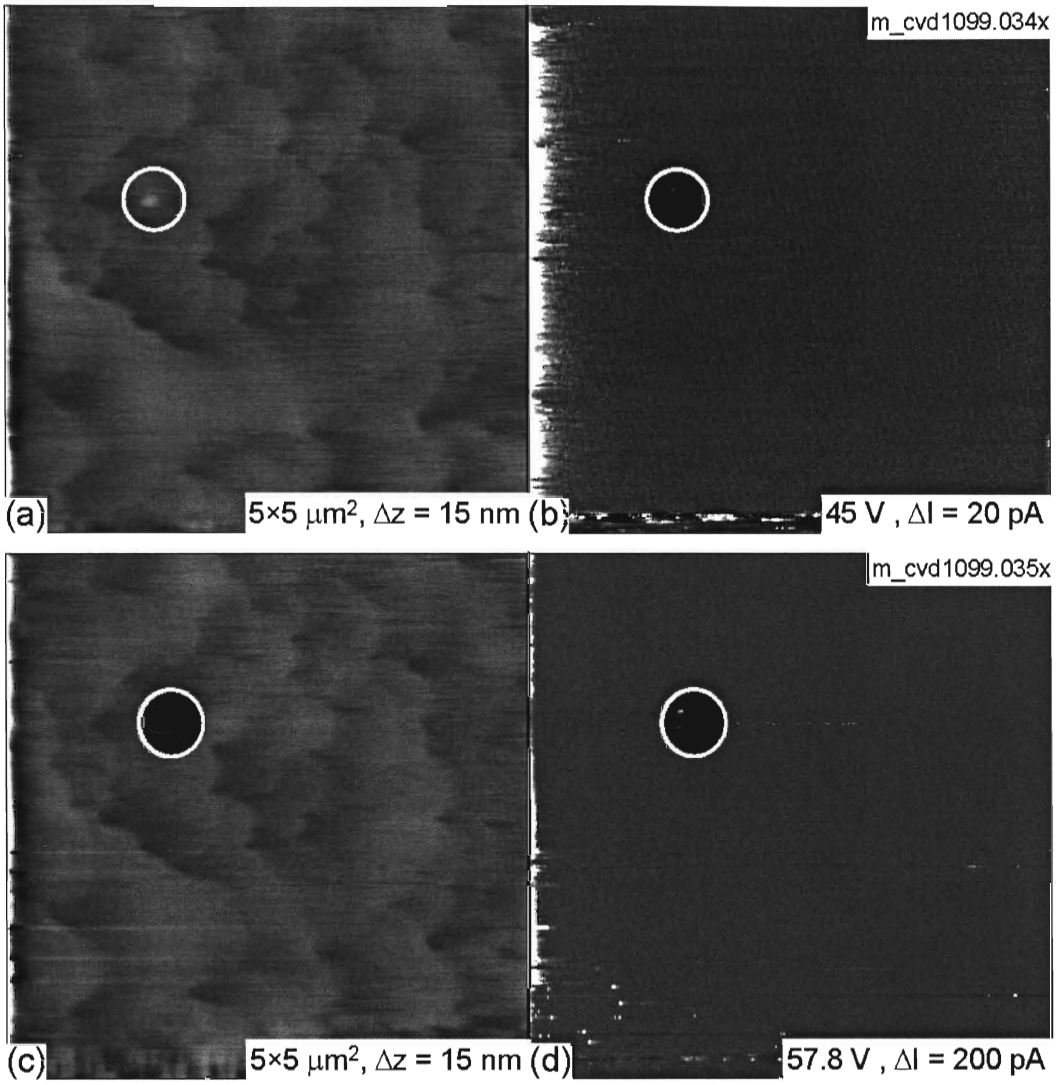

Fig 4.3: (a,c) Sample 4M topography taken using contact-mode AFM and (b,d) simultaneous current images taken using the C-AFM module. Images (c,d) were obtained immediately after (a,b) and show oxide growth followed by charging.

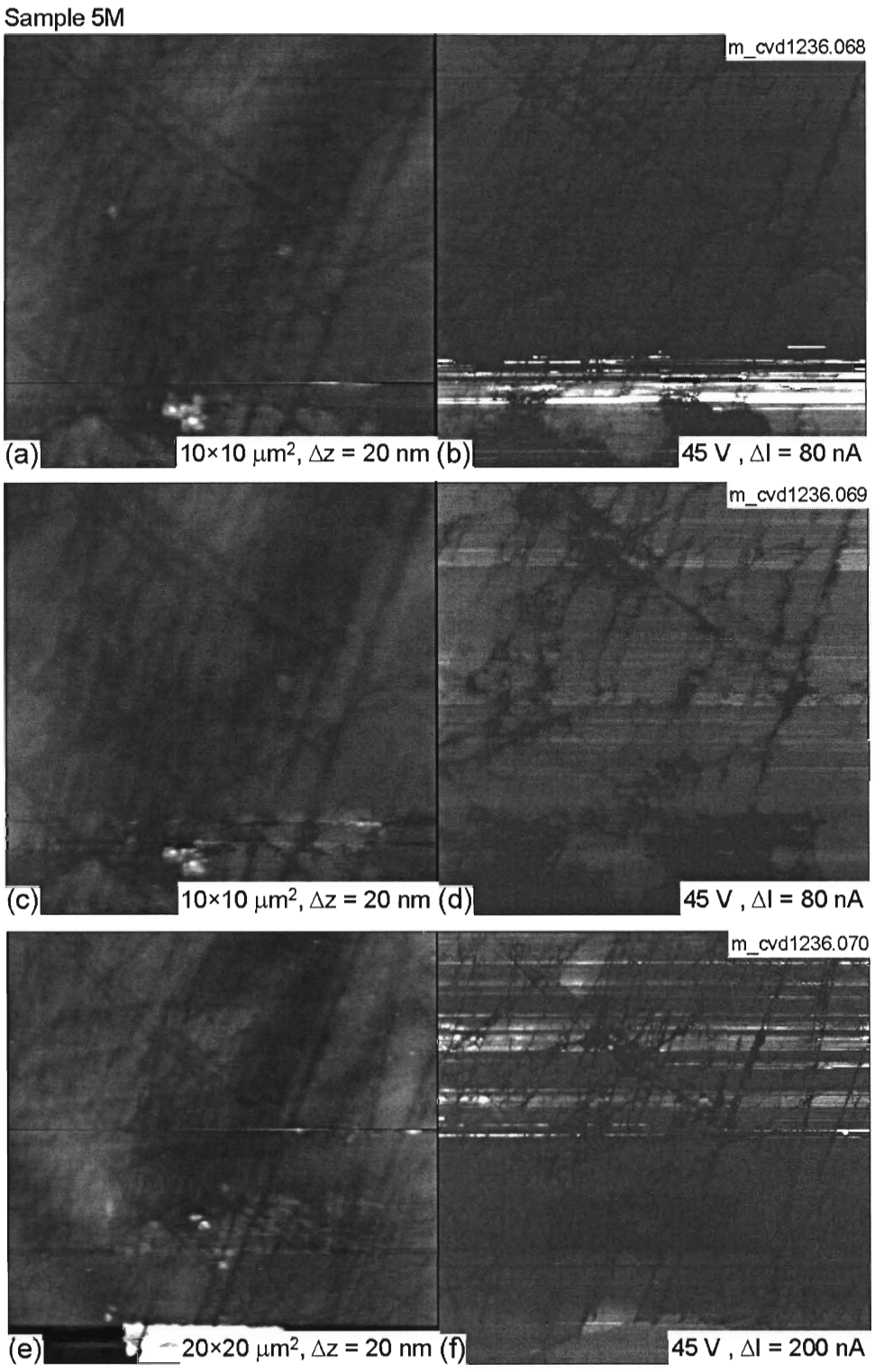

Fig 4.4: (a,c,e) Sample 5M topography taken using contact-mode AFM and (b,d,f) simultaneous current images taken using the C-AFM module.

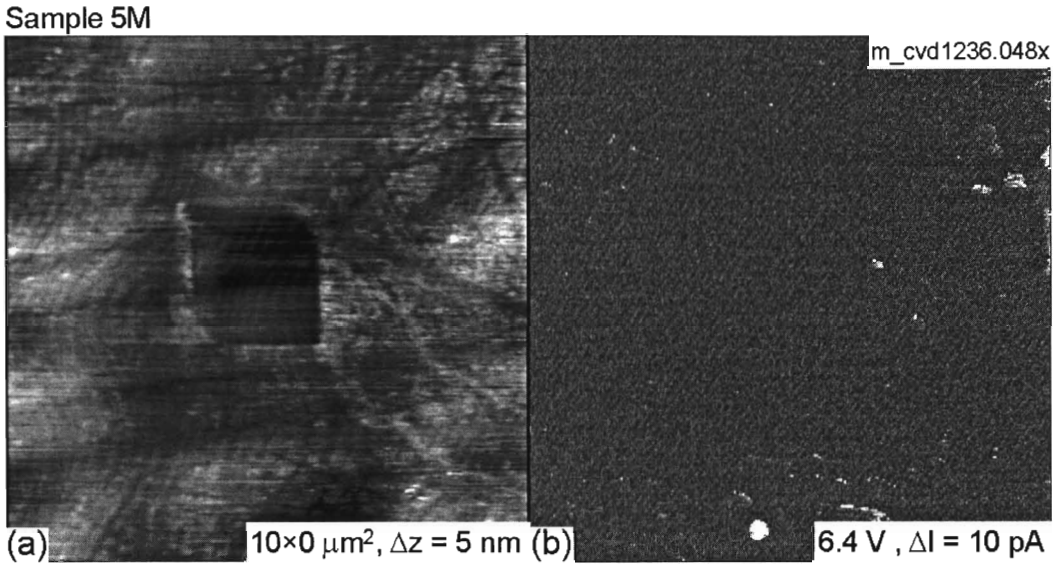

Fig 4.5: (a) Sample 5M topography taken using contact-mode AFM and (b) simultaneous current images taken using the C-AFM module.

Image #	041	042	043	044	045	046	047
Voltage	0.0	3.2	6.4	12.8	19.3	25.4	32.1

Table 4.2: List of scans of the region in Fig 4.5 (a).

References

[1] H. Morkoç. *Nitride Semiconductors and Devices* Springer-Verlag Berlin Heidelberg (1999)

[2] W.C. Johnson, J.B. Parson, M.C. Crew, *J. Phys. Chem.* **36**, 2561 (1932)

[3] H.P. Maruska, J.J. Tietjen, *Appl. Phys. Lett.* **15**, 327 (1969)

[4] J.W.P. Hsu, M.J. Manfra, S.N.G. Chu, C.H. Chen, L.N. Pfeiffer, and R.J. Molnar, *Appl. Phys. Lett.* **78**, 3980 (2001)

[5] J. Spradlin, S. Dogan, J. Xie, R. Molnar, A. A. Baski, and H. Morkoç, *Appl. Phys. Lett.* **84**, 4150 (2004)

[6] B.S. Simpkins, E.T. Yu, P. Waltereit, and J.S. Speck, *Mat. Res. Soc. Symp. Proc.* **743**, L2.4 (2003)

[7] J.W.P. Hsu, M.J. Manfra, D.V. Lang, S. Richter, S.N.G. Chu, A.M. Sergent, R.N. Kleiman, L.N. Pfieffer, and R.J. Molnar, *Appl. Phys. Lett.* **78**, 1685 (2001)

[8] B.S. Simpkins, D.M. Schaadt, E.T. Yu, and R.J. Molnar, *J. Appl. Phys.* **91**, 9924 (2002)

[9] R. Langer, J. Simon, V. Ortiz, N.T. Pelekanos, A. Barski, R. Andre M. Godlewski, *Appl. Phys. Lett.* **74**, 3827 (1999)

[10] T. Deguchi, K. Sekiguchi, A. Nakamura, T. Sota, R. Matsuo, S. Chichibu, S. Nakamura, *Jpn. J. Appl. Phys. Part 2-Lett.* **38** (8B) L914 (1999)

[11] T. Paskova, V. Darakchieva, E. Valcheva, P.P. Paskov, B. Monemar, and M. Heuken, *Phys. Stat. Sol. (b)* **240**, No. 2, 318 (2003)

[12] H.M. Ng, *Appl. Phys. Lett.* **80**, 4369 (2002)

[13] M.D. Craven, S.H. Lim, F. Wu, J.S. Speck, and S.P. DenBaars, *Appl. Phys. Lett.* **81**, 469 (2002)

[14] A. Chitnis, C. Chen, V. Adivarahan, M. Shtalov, E. Kuokstis, V. Mandavilli, J. Yang, and M.A. Khan, *Appl. Phys. Lett.* **84**, 3663 (2004)

[15] A. Chakraborty, K.C. Kim, F. Wu, J.S. Speck, S.P. DenBaars, and U.K. Mishra, *Appl. Phys. Lett.* **89**, 041903 (2006)

[16] P. Gibart, *Rep. Prog. Phys.* **67**, 667 (2004)

[17] S. Gradecak, P Stadelmann, V. Wagner, and M. Ilegems, *Appl. Phys. Lett.* **85**, 4648 (2004)

[18] Z. Liliental-Weber and D. Cherns, *J. Appl. Phys.* **89**, 7833 (2001)

[19] B. Beaumont, P. Vennéguès, and P. Gilbart, *Phys. Stat. Sol. B* **227**, 1 (2001)

[20] M.D. Craven, S.H. Lim, F. Wu, J.S. Speck, and S.P. DenBaars, *Appl. Phys. Lett.* **81**, 1201 (2002)

[21] C.Q. Chen, J.W. Yang, M.H. Wang, J.P. Zhang, V. Adivarahan, M. Gaevski, E. Kuokstis, Z. Gong, M. Su, and M. A. Khan, *J. Chem. Soc., Chem. Commun.* **42**, L640 (2003)

[22] B.M. Imer, F. Wu, S.P. DenBaars, and J.S. Speck, *Appl. Phys. Lett.* **88**, 061908 (2006)

[23] B.A. Haskell, F. Wu, M.D. Craven, S. Matsuda, P.T. Fini, T. Fujii, K. Fujito, S.P. DenBaars, J.S. Speck, and S. Nakamura, *Appl. Phys. Lett.* **83**, 644 (2003)

[24] S. Jursenas, E. Kuakstis, S. Miasojedovas, G. Kurilcik, A. Zukauskas, C.Q. Chen, J.W. Wang, V. Adivarahan, and M.A. Khan, *Appl. Phys. Lett.* **85**, 771 (2004)

[25] Ü. Özgür, X. Ni., Y. Fu, H. Morkoç, and H.O. Everitt, *Appl. Phys. Lett.* **89**, 262117 (2006)

[26] X. Ni, Y. Fu, Y.T. Moon, N. Biyikli, and H. Morkoç, *J. Cryst. Growth* **290**, 166 (2006)

[27] X. Ni, Ü. Özgür, Y. Fu, N. Biyikli, J. Xie, A.A. Baski, H. Morkoç, and Z. Liliental-Weber, *Appl. Phys. Lett.* **89**, 262105 (2006)

[28] J.W.P. Hsu, M.J. Manfra, R.J. Molnar, B. Heying, and J.S. Speck, *Appl. Phys. Lett.* **81**, 79 (2002)

[29] B.S. Simpkins, E.T. Yu, P. Waltereit, and J.S. Speck, *Mater. Res. Soc. Symp. Proc.* **743**, L2.4 (2003)

[30] J. Spradlin, S. Dogan, J. Xie, R. Molnar, A.A. Baski, and H. Morkoç, *Appl. Phys. Lett.* **84**, 4150 (2004)

[31] J.C. Moore, K.A. Cooper, J. Xie, H. Morkoç, and A.A. Baski, *Proc. SPIE* **6121**, 61210J-1 (2001)

[32] D.N. Zakharov, Z. Liliental-Weber, B. Wagner, Z.J. Reitmeier, E.A. Preble, and R.F. Davis, *Phys. Rev. B* **71** 235334 (2005)

[33] J.E. Northrup, *Appl. Phys. Lett.* **78**, 2288 (2001)

[34] J.C. Moore, V. Kasliwal, A.A. Baski, X. Ni, Ü. Özgür, H. Morkoç, *Appl. Phys. Lett.* **90**, 011913 (2007)

[35] S. Haffouz, H. Lahrèche, P. Vennéguès, P. de Mierry, B. Beaumont, F. Omnès, and P. Gibart, *Appl. Phys. Lett.* **73**, 1278 (1998)

[36] E. Monroy, F. Calle, E. Muñoz, B. Beaumont, F. Omnès, and P. Gibart, *Phys. Stat. Sol. (a)* **76**, 141 (1999)

[37] T. Wang, Y. Morishima, N. Naoi, S. Sakai, *J. Cryst. Growth* **213**, 188 (2000)

[38] S. Sakai, T. Wang, Y. Morishima, Y. Naoi, *J. Cryst. Growth* **221**, 334 (2000)

[39] X. L. Fang, Y.Q. Wang, H. Meidia, and S. Mahajan, *Appl. Phys. Lett.* **84**, 484 (2004)

[40] J. Xie, Y. Fu, X. Ni, S. Chevtchenko, and H. Morkoç, *Appl. Phys. Lett.* **89**, 152108 (2006)

[41] J.L. Pau, C. Rivera, E. Muñoz, E. Calleja, U. Schühle, E. Frayssinet, B. Beaumont, J.P. Faurie, and P. Gibart, *J. Appl. Phys.* **95**, 8275, (2004)

[42] S.C. Wei, Y.K. Su, S.J. Chang, Shi-Ming Chen, and Wen-Liang Li, *IEEE Trans. Electronic Devices* **52**,1104 (2005)

[43] J. Xie, Ü. Özgür, Y. Fu, X. Ni, H. Morkoç, C.K. Inoki, T.S. Kuan, J.V. Foreman, H.O. Everitt, *Appl. Phys. Lett.* **90**, 041107 (2007)

[44] Y.T. Moon, J. Xie, C. Liu, Y. Fu, X. Ni, N. Biyikli, K. Zhu, F. Yun, H. Morkoç, A. Sagar, R.M. Feenstra, *J. Cryst. Growth* **291**, 301 (2006)

[45] J.C. Moore, J.E. Ortiz, J. Xie, H. Morkoç, A.A. Baski, *J. Phys: Conf. Ser.* **61**, 90 (2007)